# Convective and Stratiform Components of a Winter Monsoon Cloud Cluster Determined from Geosynchronous Infrared Satellite Data

By Stanley B. Goldenberg[1], Robert A. Houze, Jr. and Dean D. Churchill

*Department of Atmospheric Sciences, University of Washington, Seattle, WA 98195*
*(Manuscript received 8 June 1989, in revised form 13 November 1989)*

## Abstract

A technique originally devised by Adler and Negri (1988) for estimating the convective and stratiform precipitation areas and amounts of mesoscale convective cloud systems from infrared satellite imagery has been applied to a large cloud cluster observed over the South China Sea during the Winter Monsoon Experiment (WMONEX). The technique was modified to obtain agreement with a previous analysis of ground-based radar data obtained in a limited part of the cluster. The modifications included altering the method for identifying convective cells in the satellite data, accounting for the extremely cold cloud tops characteristic of the WMONEX region and modifying the threshold infrared temperature for the boundary of the stratiform rain area.

After obtaining agreement with the radar analysis over a limited portion of the cluster's area and lifetime, the satellite technique was applied to the entire cluster over its full lifetime. The locations of the convective and stratiform rain areas found in this extended analysis were consistent with WMONEX research ship and aircraft data of the cluster. The evolution of total convective and stratiform precipitation indicated by the satellite analysis over the cluster's lifetime was qualitatively consistent with previous radar analyses of other equatorial cloud clusters, except that this cluster appears to have developed a particularly strong stratiform component during its mature stage.

The successful application of the Adler and Negri technique to the WMONEX cloud cluster provides encouragement for the use of this method; to develop satellite-based climatologies of the convective-stratiform internal structure of cloud clusters over large regions of the tropics where radar data are not typically available. It also appears that this technique will be a useful complement to future spaceborne precipitation-measuring radar systems.

## 1. Introduction

Much of the precipitation in both midlatitudes and the tropics falls from mesoscale convective systems, which are recognizable by their cloud shields seen in infrared (IR) satellite pictures. In the tropics, these mesoscale cloud systems have often been referred to as "cloud clusters" (*e.g.*, Houze and Betts, 1981). While in midlatitudes, the most intense of such cloud shields, which satisfy criteria regarding their size, shape, duration, and coldness, have been called "mesoscale convective complexes (MCCs)" (Maddox, 1980). Generally, the cloud shield is a few hundred kilometers in horizontal dimension, and the underlying precipitation area is on the order of 100 km or more in at least one horizontal dimension. Although these mesoscale systems begin as complexes of convective storms, they develop large regions of stratiform precipitation during their lifetimes. 25–50 % of the total rain reaching the ground from such systems is typically stratiform (Houze and Hobbs, 1982; Leary, 1984). It is useful to distinguish the convective and stratiform components of these cloud systems; since the physics and dynamics of the air motions and precipitation growth in the convective and stratiform regions are fundamentally different. As discussed by Houze (1989), the mesoscale organization of a mesoscale system is indicated by the patterns of convective and stratiform rain, and the microphysical processes as well as the vertical distributions of vertical air motion and diabatic heating are quite different in the convective and stratiform regions. The stratiform region has also been shown to be the location of the development of a mesoscale vortex at mid-levels (*e.g.*, Houze, 1977; Gamache and Houze, 1982, 1985; Leary and Rappaport, 1987), and that this vortex development process, which begins in the

[1]Present Affiliation: Sar Shalom Hebrew Academy, 4751 NW 24th Court Waterdale Lakes, FL 33313, USA.

stratiform region, may lead to the long lifetimes of MCCs (Zhang and Fritsch, 1988).

Although it appears for these reasons to be important to distinguish the convective and stratiform regions of mesoscale convective systems, it is usually difficult to do so because this distinction is most readily made where high-quality radar data are available. If the distinction between convective and stratiform regions of mesoscale convective systems could be made in satellite observations, then the convective and stratiform components of cloud systems over regions not covered by surface-based radar could be observed. It would then be possible to investigate the convective-stratiform structure of mesoscale cloud systems over the widespread areas, particularly remote tropical oceans and land masses. Eventually, some form of satellite-borne radar will probably be used to investigate mesoscale cloud systems globally. For example, a low-inclination, low-orbit satellite carrying precipitation radar, passive microwave and IR instrumentation has been suggested for the Tropical Rainfall Measuring Mission (TRMM; see Simpson *et al.*, 1988). This type of satellite is probably the best spaceborne rainfall-measuring system that can be expected in the foreseeable future. However, even it is limited. In particular, it will not provide wide coverage at any given time, but rather will probably sample rainfall over small areas at fairly long intervals of time to achieve a climatology. Conventional geosynchronous satellites with IR and visible-wavelength radiometers will continue as the primary means of obtaining continuous daily coverage over wide areas, with the TRMM-type of satellite providing important calibration points. Therefore, it is important to develop ways that IR observations can be used to complement the TRMM-type of satellite measurements. In this paper, we examine the use of geosynschronous IR satellite observations to determine the convective and stratiform components of a tropical cloud cluster.

Recently, Adler and Negri (1988) have proposed a technique that uses geosynchronous IR data to distinguish between the convective and stratiform components of mesoscale convective cloud systems that have extensive cirriform tops. They tested their algorithm, referred to as the Convective-Stratiform Technique (CST), on data from the Geosynchronous Operational Environmental Satellite (GOES) IR (10.5–12.6 $\mu$m) channel obtained during four days of the second Florida Area Cumulus Experiment (FACE). They inferred rainfall areal coverage and amount and resolved it into convective and stratiform components in general agreement with radar- and raingauge-observed rainfall. The technique showed the greatest skill in the determination of the convective and stratiform precipitation for scales on the order of $10^4$ km$^2$ (*i.e.*, approximately 1° latitude × 1° longitude) or more, although in some cases, the horizontal distribution of the convective and stratiform components of precipitation also conformed closely with the radar-observed horizontal precipitation structure on smaller (*i.e.*, convective) scales.

The purpose of our study is to adapt the Adler-Negri CST to the analysis of the horizontal precipitation structure of cloud clusters over an equatorial ocean area. The successful performance of this exercise has both an immediate benefit and long-term implications. The immediate benefit is that we are able to use the modified CST to extend previous analysis of a cloud cluster observed in the Winter Monsoon Experiment (WMONEX). This cloud cluster has been described by Houze *et al.* (1981b), Johnson and Priegnitz (1981), Warner (1982), Johnson and Kriete (1982), Johnson (1982), Johnson and Young (1983), and Churchill and Houze (1984a,b). The cluster was observed off the northern coast of Borneo by coastal radar during its early stages. Then it moved out to sea, where it was further observed by a research ship and by two research aircraft. Churchill and Houze (1984a, hereafter CH) used the coastal radar data to distinguish the development of convective and stratiform precipitation in the cluster. However, their analysis was limited to the early period, before the system moved out of range of the coastal radar. By applying an appropriately modified version of the Adler-Negri CST to IR imagery from geosynchronous-satellite observations, we are able to extend this precipitation analysis to the entire history of the cloud cluster. The ship and aircraft data available during the later period of the cluster's lifetime, moreover, allowed the locations of convective and stratiform precipitation identified by the CST-extended analysis to be checked by *in situ* observations.

The longer-term benefit of this work is that an extended version of the Adler-Negri CST affords an opportunity to determine the climatology of the convective-stratiform structure of tropical cloud clusters. Previous tropical cloud cluster climatologies based on satellite data (Martin and Schreiner, 1981; Williams and Houze, 1987) have determined sizes, shapes, brightness, lifetimes, tracks, mergers, splits, diurnal variability and other features of clusters in a statistical manner. However, a climatology of the convective-stratiform substructure of cloud clusters has not yet been accomplished. The present study can be regarded as an attempt to calibrate the CST for wider application in a climatological study. The WMONEX data set used here is one of the few available ground-truth data sets for which ground-based radar, ship-based surface and rawinsonde observations, and research aircraft data can all be compared directly with the results of the CST. We therefore take full advantage of these special observations to test and make adjustments, where necessary, to

the CST. A direct transferal of the original CST to equatorial regions, as will be shown, is not possible because of the higher, colder cloud tops characterizing the equatorial zone, especially the region of WMONEX.

After describing the data sources in Sec. 2, the modifications to the Adler-Negri CST necessary to obtain consistency between the CST results and the WMONEX ground-truth data will be indicated in Sec. 3. In Sec. 4, the modified CST will then be applied to a limited portion of the cloud cluster, namely the portion studied by CH. Close agreement between the convective and stratiform rain areas, and amounts estimated by the CST and found from radar data by CH for this limited portion of the cluster, is obtained. This agreement is considered as justification for applying the modified CST to the entire area and lifetime of the cluster in Sec. 5, thus using the satellite data to extend the earlier WMONEX studies to the portions of the cluster occurring outside the special observing network. New conclusions drawn concerning the extension of previous results to the whole cluster and implications of this successful application of the CST for its future application in climatological studies are discussed in Sec. 6.

## 2. Data

### *a. WMONEX observations*

The data used in this study were obtained during WMONEX on 9–10 December 1978. Details of the observational facilities and a map of the data network are given by CH. Briefly summarized, the data network consisted of the following items: a weather radar operated by the Massachusetts Institute of Technology (MIT) during MONEX was located at Bintulu on the north coast of Borneo; three Soviet research ships in the South China Sea arranged in a triangle north of Borneo, just northwest of the area of radar observations, provided surface weather observations and rawinsonde data; a WP-3D ("P3") research aircraft of the U.S. National Oceanic and Atmospheric Administration and the Electra research aircraft of the U.S. National Center for Atmospheric Research flew missions over the southern South China Sea at altitudes of 7.8 and 6.3 km, respectively; and visible and IR satellite imagery were provided by observations from the Japanese Geosynchronous Meteorological Satellite (GMS-1).

### *b. Cloud Cluster B and the strategy of the study*

In this paper, we rely on the analysis of the Bintulu radar data presented by CH. In particular, we focus on the large mesoscale cloud system referred to as "Cluster B" by CH. According to their analysis, cluster B formed just prior to 1730 GMT 9 December 1978 and dissipated shortly after 1130 GMT 10 December. CH used the digitized reflectivity data from the WR-73 C-band weather radar located at Bintulu (see Fig. 1) to determine precipitation rates at 3 km altitude using the $Z_e-R$ relationship of Hudlow *et al.* (1979).[1] Employing an objective criterion that identified convective cores as those echoes whose rainfall rates are at least twice the average of the surrounding rain rates, CH then partitioned radar-derived precipitation areas and amounts, from 1200 GMT on 9 December to 0330 GMT on 10 December, into convective and stratiform components.

Figure 1 shows the general area for the present study. Also shown are the area of coverage for the MIT radar at Bintulu (Houze *et al.*, 1981a, b; CH; Geotis and Houze, 1985), the region of the cluster B radar analysis of CH (dotted line), and the limited region over which the CST and radar results are compared in Sec. 4 (dashed line). It was necessary to restrict the area for the CST-radar comparison because the cluster gradually moved out of the range in which quantitative radar observations were obtained. In addition, the radar coverage was severely restricted at low levels in certain sectors because of beam blockage problems (Geotis and Houze, 1985). The boundaries of the area of comparison indicated by the dashed line in Fig. 1 were arrived at by examining the 3 km level radar-echo patterns for cluster B from CH and the 24-day WMONEX low-level radar rainfall analysis from Geotis and Houze (1985). The area was confined to those regions for which there appeared to be good radar coverage for cluster B. Data over land, where the radar data were particularly inadequate, were not included, and except for a small portion on the boundary of the southwest sector, radar data from the southwest region where the blockage was worst, were not used in the CST-radar comparison.

After the limited-area comparison of the radar and CST analyses is presented to indicate the performance of the CST in Sec. 4, the CST is applied in Sec. 5 to a larger area containing the entire cluster (shaded region in Fig. 1). Observations from the research ship *Ak. Korolov* (see Fig. 1 for location) and from the two research aircraft obtained generally northwest of the area of radar observations allowed some *in situ* verification of the locations of convective and stratiform areas.

### *c. Characteristics of the satellite data*

The satellite data set used in this study is a subset of the WMONEX satellite data set obtained from the University of Wisconsin and used by CH and

[1] $Z_e=230R^{1.25}$, where $Z_e$ is the effective radar reflectivity factor in $mm^6/m^3$, and $R$ is rainfall rate in $kg\,m^{-2}\,h^{-1}$. This relationship was used by CH in their radar study of cloud cluster B. Houze *et al.* (1981a) showed that the radar measurements are accurate to 1–2 dBZ in comparison with airborne radar.

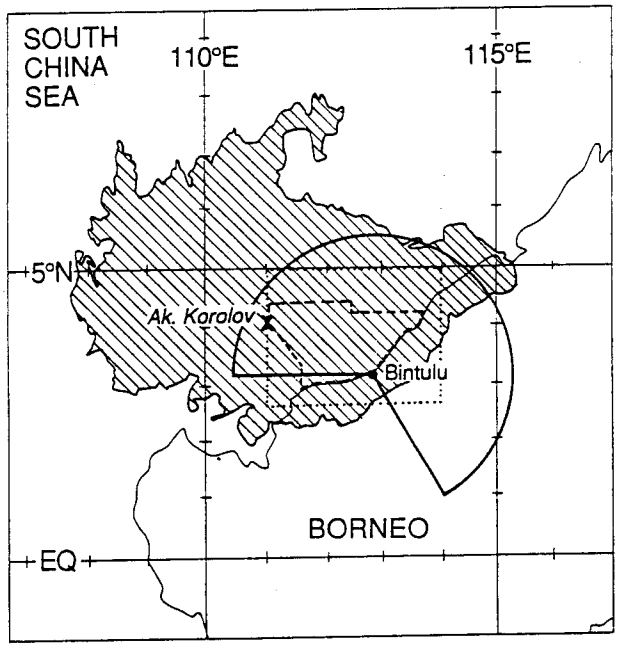


Fig. 1. Cloud cluster B analysis domains and composite of the cirrus cloud shield associated with cluster B. The shaded region is the union of the cirrus shields (defined as the areas where the satellite IR temperature is $\leq 245°K$) seen in individual images during the time period 1733 GMT through 1133 GMT, 9–10 December 1978. Horizontal coverage of MIT land-based radar located at Bintulu is shown by the solid line. Radar data from most of the southwestern sector were not used due to beam blockage. The location of the Soviet ship *Ak. Korolov* is indicated by an *X*. The region examined by CH in their analysis of the MIT radar data is outlined by the dotted line. The area over which the CST results for cluster B are compared with the radar results in Secs. 3 and 4 is indicated by the dashed line.

Williams and Houze (1987). We have used only the data for 9 and 10 December and for the restricted spatial domain encompassing cluster B (see Fig. 1). Digitized data from the GMS-1 IR channel on 9 December 1978 (1733, 2033, 2203, 2233, 2303, and 2333 GMT) and 10 December 1978 (0233, 0533, 0833, 1003, 1033, 1103, and 1133 GMT) are used. The north-south resolution of the GMS-1 IR data in the vicinity of cluster B is about 5 km. The east-west resolution, however, is about 3 km as a result of oversampling in that direction.

Accurate navigation of the GMS-1 data is a recognized problem (Martin and Howland, 1986; Williams and Houze, 1987). In an attempt to minimize location errors in the satellite data, especially for use in the radar-CST comparisons in Sec. 4, we have refined the navigation as much as possible. This was accomplished by comparing features in IR imagery and CST results with features in the CH analyses of data from the Bintulu and P3 radars, and by comparing locations of geographical features with visible satellite imagery coastal outlines. The final navigation errors of the satellite data are probably $<15$ km for the image times when radar data was available (1733 through 0233 GMT 9–10 December for Bintulu data, and 1003 GMT 10 December for P3 radar data) and as high as 30 km for other data times.

## 3. The modified Convective-Stratiform Technique

### *a. Flowchart*

In analyzing the GMS-1 IR data, we follow the basic CST algorithm of Adler and Negri (1988), henceforth referred to as AN. Figure 2 shows a flowchart of the general technique. In this study, we follow this flowchart incorporating the modifications to their procedure listed in the far-right column of Fig. 2.

### *b. Location of convective cores in the infrared imagery*

The first step in the CST (see Fig. 2) is to locate convective cores. To accomplish this, each satellite image is analyzed independently. The satellite IR brightness temperature ($T_b$) field is searched for relative minima ($T_{min}$), each consisting of either a single-pixel minimum, or the centroid of a multi-pixel minimum. Next, a "slope parameter" ($S$) is calculated for each $T_{min}$ to measure the strength of the minimum. For our application, the slope parameter used by AN had to be corrected for the differences in data-bin size between the GOES [8.0 km (north-south) by 3.1 km (east-west)] and GMS-1 [5.2 km (north-south) by 2.1 km (east-west)] IR data. We have revised the slope parameter further to remove the directional bias contained in their definition. The slope parameter used for this study is given by:

$$S = \frac{\bar{\Delta}}{4}\left[\frac{T_{i-2,j} + T_{i+2,j} + 2\,(T_{i-1,j} + T_{i+1,j}) - 6T_{i,j}}{4\Delta_{EW}} + \frac{T_{i,j-1} + T_{i,j+1} - 2T_{i,j}}{\Delta_{NS}}\right], \quad (1)$$

where $i,j$ refers to the position of the pixel for which $S$ is being calculated; $\Delta_{EW}$ and $\Delta_{NS}$ are the GMS-1 east-west and north-south resolutions, respectively; and $\bar{\Delta}$ is the average GOES distance (from AN) to the six surrounding pixels. Twice as many pixels are used for the calculation in the east-west ($i$) as in the north-south ($j$) direction to be consistent with the difference in resolution. Further details related to the development of this expression are given in Appendix A.

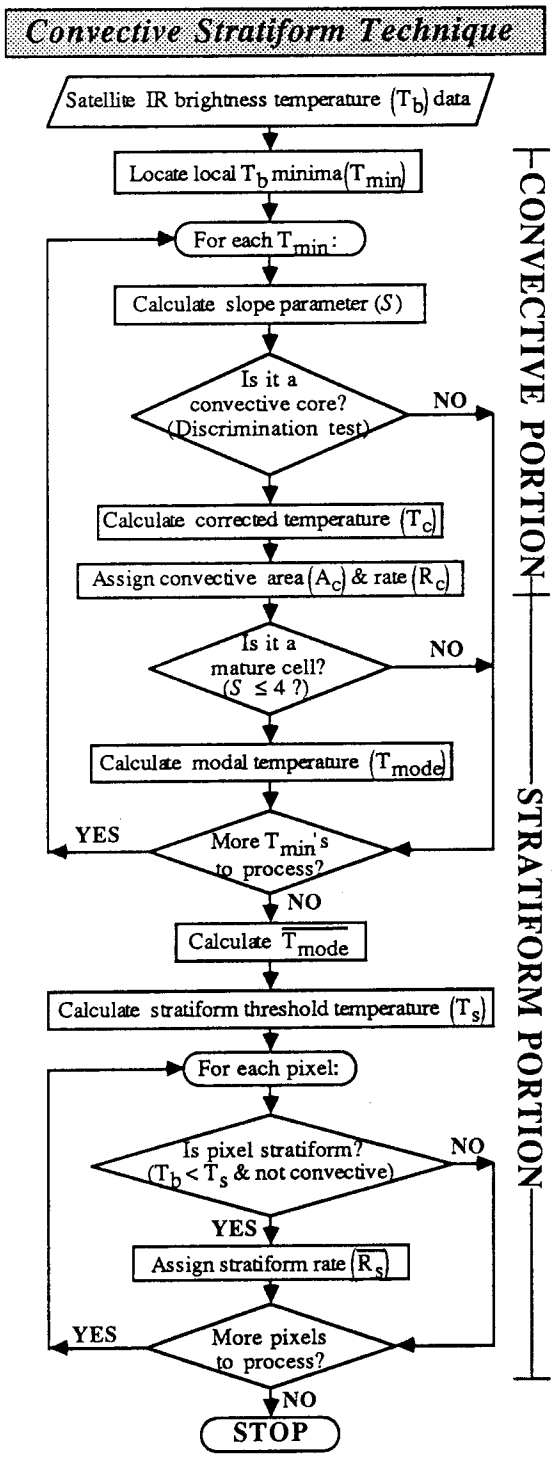


| | FACE APPLICATION (Adler & Negri, 1988) | CLUSTER B Application |
|---|---|---|
| | GOES-E Resolution: 8.0 x 3.1 km | GMS-1 Resolution: 5.2 x 2.1 km |
| | Simple difference between $T_{min}$ & mean of six surrounding $T_b$'s | Adjusted for new resolution & corrected for directional bias [ Eq. (1) ] |
| | Linear discrimination line [Eq. (2)] | Exponential discrimination line [Eq. (3) ] |
| | According to GOES resolution | According to GMS-1 resolution [Eq. (5) ] |
| | Parameters from 1-D model runs for Florida | Parameters from 1-D model runs for cluster B [ Eqs. (4) & (10) ] |
| | Weighted mean of $T_{mode}$'s [Eq. (13)] $T_s = \overline{T_{mode}}$ | Mean of modal grid [Eq. (14)] $T_s = \overline{T_{mode}} + 7$ K |

Fig. 2. Flowchart of CST. Also shown in the right two columns are brief descriptions of differences between original CST as applied to FACE data (Adler and Negri, 1988) and modified CST (described in Sec. 3) as applied to cloud cluster B data in current study.

The ($T_{min}$'S) pairs are then compared to an empirical "discrimination line" to distinguish which $T_{min}$'s are associated with convective cores. According to AN, a minimum is said to indicate the location of a convective core if

$$S \geq 0.568(T_{min} - 217). \quad (2)$$

This condition was obtained *via* a subjective analysis of digital radar echoes and GOES visible and IR-channel imagery data to separate points designated as convective cores from those identified with thin cirrus. Their discrimination line is based on the assumption that a large $S$ combined with at least a moderately low $T_{min}$ generally indicates ac-

tive convection. The required magnitude for $S$ decreases however, for the colder cloud tops, which are generally associated with intense, mature cells with spreading anvils which experience some flattening at near-tropopause height.[2]

The discrimination line of AN was modified for the present application because the coldest cloud-top temperatures in the WMONEX region were typically 15 to 20°K lower than for the FACE data examined by AN. The coldest cloud tops noted by AN were near 200°K, whereas for cluster B, tops were as cold as 180°K. The discrimination line of AN [Eq. (2)] allows all $T_{min}$<217 K, *regardless of the value for S*, to be selected as convective cores. Thus, in cloud shields colder than 217°K (common in the WMONEX data), many spurious convective cores are selected from even minor perturbations in the $T_b$ field. To assist in the construction of a revised discrimination line for use in the current application, plots of ($T_{min}$, $S$) pairs for cluster B were checked against convective cell locations in the CH radar analysis. We sought a discrimination line that was similar to that of AN in portions of the temperature range that they considered, but that rejected spurious centers in the application to the WMONEX data. We found that this result could be accomplished by an exponential form, rather than the linear form used by AN. The new relationship is given by

$$S \geq exp[0.0826(T_{min} - 207)]. \quad (3)$$

The utility of this relationship is illustrated by the following examples.

The status assigned to each of the relative minima in the $T_b$ field for cluster B at 2203 GMT on 9 December and 0533 GMT on 10 December, respectively, by the linear equation (2) and the exponential relation (3), is shown in Fig. 3. The first time (Fig. 3a), according to the analysis of CH, was during the period in which some of the most intense convection occurred. The second time (Fig. 3b), according to the radar analysis in CH and visible satellite imagery, was during the period when the precipitation in cluster B was mostly stratiform. Figures 4a and b are plots of $T_{min}$ vs. $S$ for 2203 GMT and 0533 GMT, respectively, with the scale for $S$ being logarithmic and showing both the linear (2) and exponential (3) discrimination curves. It can be seen that the convective cores selected for 2203 GMT (Figs. 3a and 4a) are barely affected by the implementation of the new discrimination line (3). However, a large number of the $T_{min}$ values that pass as convective cores for 0533 GMT (Figs. 3b and 4b) using (2) re-

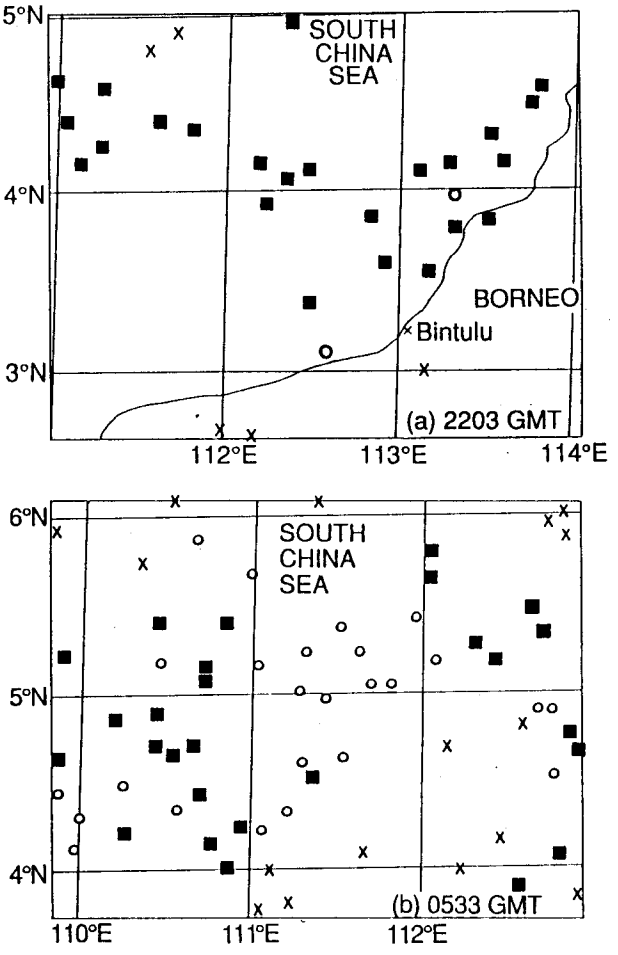


Fig. 3. Location and status of every relative minimum ($T_{min}$) in the satellite IR temperature ($T_b$) field for cloud cluster B at (a) 2203 GMT on 9 December and (b) 0533 GMT on 10 December 1978. Crosses indicate $T_{min}$'s which are rejected as convective cores by both the linear and exponential discrimination lines [Eqs. (2) and (3), respectively]; open circles show points which are passed by (2) but rejected by (3); and squares show points which are passed by (2) and (3). The region shown in (a) is the same as the region enclosed by the dotted line in Fig. 1. The region shown in (b) is shifted from the dotted-line region shown in Fig. 1 to include more of the cluster at 0533 GMT.

[2]It is recognized that an area of excessively low infrared cloud-top temperature may not be directly located over the convection at lower levels (*e.g.*, Houze, 1977; Heymsfield and Fulton, 1988; Zipser, 1988). However, the CST does not purport to give the exact location of the convection, but rather the approximate intensity and area covered by convection. It is assumed that a bright area in the infrared pattern that satisfies the criteria described in this section is typically at least indirectly related to the presence of strong convection and has an intensity that is somewhat correlated with the area covered by convection. Also, it may be that the CST would have difficulty characterizing rapidly moving squall lines, such as those with which Houze (1977) and Zipser (1988) were concerned, which are characterized by highly sloping convection and intense trailing-stratiform cloud and precipitation.

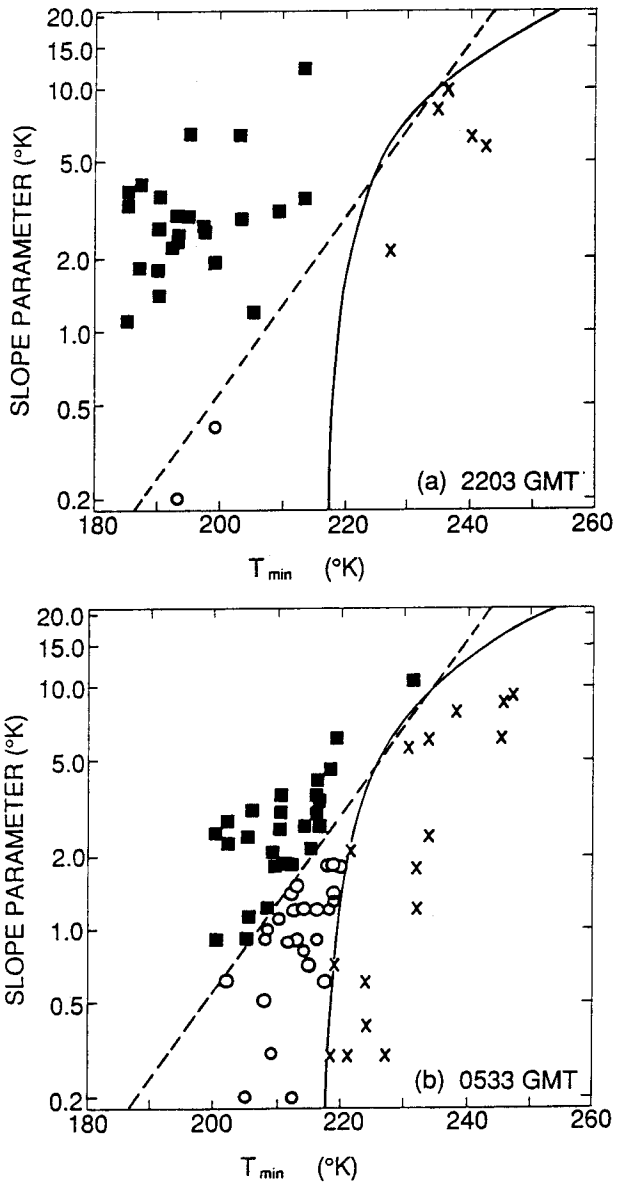


Fig. 4. $T_{min}$ vs. $S$ for (a) 2203 GMT and (b) 0533 GMT. The scale for $S$ is logarithmic. Solid curved line is linear discrimination line (2) from Adler and Negri (1988). Dashed straight line is exponential discrimination line (3) derived for cluster B application. Status of each $T_{min}$ is indicated by cross, open circle or square as in Fig. 3. $T_{min}$'s for (a) and (b) are for the same regions shown in Figs. 3a and b, respectively.

sult from minor variations in the overall cold temperature of the cloud shield and probably not from the presence of actual convective cores. Many of these $T_{min}$'s for 0533 GMT fall in the triangular-like region between the lines for (2) and (3) on Fig. 4b, indicating that they are correctly rejected as convective cores by the exponential discrimination line (3), although they would have passed as convective cores using the AN linear discrimination line (2).

*c. Estimation of area covered by convective precipitation*

The next step in the CST (see Fig. 2) is to assign areal coverage of convective precipitation [$A_{ci}$ (km$^2$)] to each of the cores selected through the screening process described in Sec. 3b. The index i refers to the $i$-th core. To assign the area, we follow AN in assuming that $\ln(A_{ci})$ is directly proportional to cell-top height, which is indicated by cloud-top temperature.

The linear relationship of $\ln(A_{ci})$ to the cloud-top temperature of the i-th convective core can be written

$$\ln(A_{ci}) = aT_{ci} + b, \tag{4}$$

where $a$ and $b$ are constants, and where, as in AN, $T_{min}$ is replaced by the variable $T_{ci}$, which is the cloud-top temperature of the $i$-th convective core corrected for the difference in resolution between the satellite data and the one-dimensional cloud model of Adler and Mack (1984). This model is used in some of the following considerations, and the correction, which was obtained by AN for use with the GOES resolution and is adjusted here for the GMS-1 resolution, is given by

$$T_{min} - T_c(^\circ K) = \left\{ \begin{array}{ll} 0.113T_{min} - 22.6, & \\ \quad T_{min} > 200\ K & \\ 0, & \\ \quad T_{min} \leq 200\ K & \end{array} \right\}. \tag{5}$$

A further explanation about the adjustment given in (5) is presented in Appendix B.

Adler and Mack (1984) used a one-dimensional cumulus model to make several calculations for the environment of Florida convection and compared these model results with radar observations of Florida convection. From these comparisons, AN concluded that, if the area of the model updraft, $A_u$, was expressed as

$$\ln(A_u) = a'T_c + b', \tag{6}$$

where $a'$ and $b'$ are constants, then the slope in (4), derived by a log-linear fit of the Florida radar convective area observations, was approximately equal to the slope in (6), derived from a log-linear fit of the model results. Thus, for their study, AN let

$$a = a'. \tag{7}$$

Runs were carried out for the purpose of this study with the same one-dimensional model, but with a WMONEX sounding for 1800 GMT on 9 December 1978 in the vicinity of cluster B (taken at *Ak. Korolov*; see Fig. 1 for location). These calculations yielded a slope very similar to that obtained

by AN. For WMONEX, the value of $a'$ is -0.0492, as compared to their value of -0.0465 for Florida. For consistency with their work, we decided to use their value of $a'$ and assume that $a$=$a'$, as in (7).

It remains to determine the intercept $b$ in (4) for the cluster B application. As a first guess, one can use the value of $b$=15.27 determined by AN for Florida convection. This AN convective area relationship is shown in Fig. 5a. With this value of $b$, together with their value of $a$, we have used (4) to assign $A_{ci}$ to each core, centering the areal assignment on the location of the $T_{min}$ associated with the core. Then, for each of the satellite data times from 1733 GMT to 0533 GMT on 9–10 December, we have obtained the CST-derived estimate of the total area covered by convective rainfall, $A_T$, by summing up all the $A_{ci}$'s for that time, with overlapping areas counted only once. From CH, we have an estimate of $A_T$ based on radar data in cluster B for the same times. The $A_T$ values computed using (4) are compared to the CH values in Table 1. The CST values are slightly higher for most of the image times, but this is to be expected. Because of radar attenuation and beam-blockage problems, the CST-derived areas, if "correct", should be equal to or greater than the radar-derived areas. It is difficult to quantify what these differences should be from these data, but certainly the agreement here appears to be adequate enough to adopt (4) with AN's values of $a$ and $b$ as an acceptable way of estimating the area of rain associated with a convective core identified by the CST.

*d. Rain rate in the convective area*

To obtain an estimate of the average rain rate, $R_{ci}$(kg m$^{-2}$ h$^{-1}$), in the area $A_{ci}$ associated with the $i$-th core, we continue to follow AN by using the model of Adler and Mack (1984) to calculate the time rate of fallout of condensed water mass $V_{ri}$(kg h$^{-1}$) as a function of $T_{ci}$. This quantity is related to $R_{ci}$ and $A_{ci}$ according to

$$R_{ci} = \frac{V_{ri}}{A_{ci}}. \tag{8}$$

$R_{ci}$ can then be calculated from $V_{ri}$ given by the model run for a cell of cloud-top temperature $T_{ci}$ in the WMONEX environment and from $A_{ci}$, where $A_{ci}$ is given by (4). Our procedure in calculating $R_{ci}$ is first to obtain a log-linear fit to the results from several model runs (described in Sec. 3c) for $V_{ri}(T_{ci})$ in the WMONEX environment, representing $V_{ri}$ as

$$\ln(V_{ri}) = c\,T_{ci} + d. \tag{9}$$

Each of the runs used the same sounding data and differed only in the model updraft radius. The different updraft radii and log-linear fit are plotted in Fig. 5b. The fit (shown in Fig. 5b) to the results from the WMONEX runs yields values of -0.0622

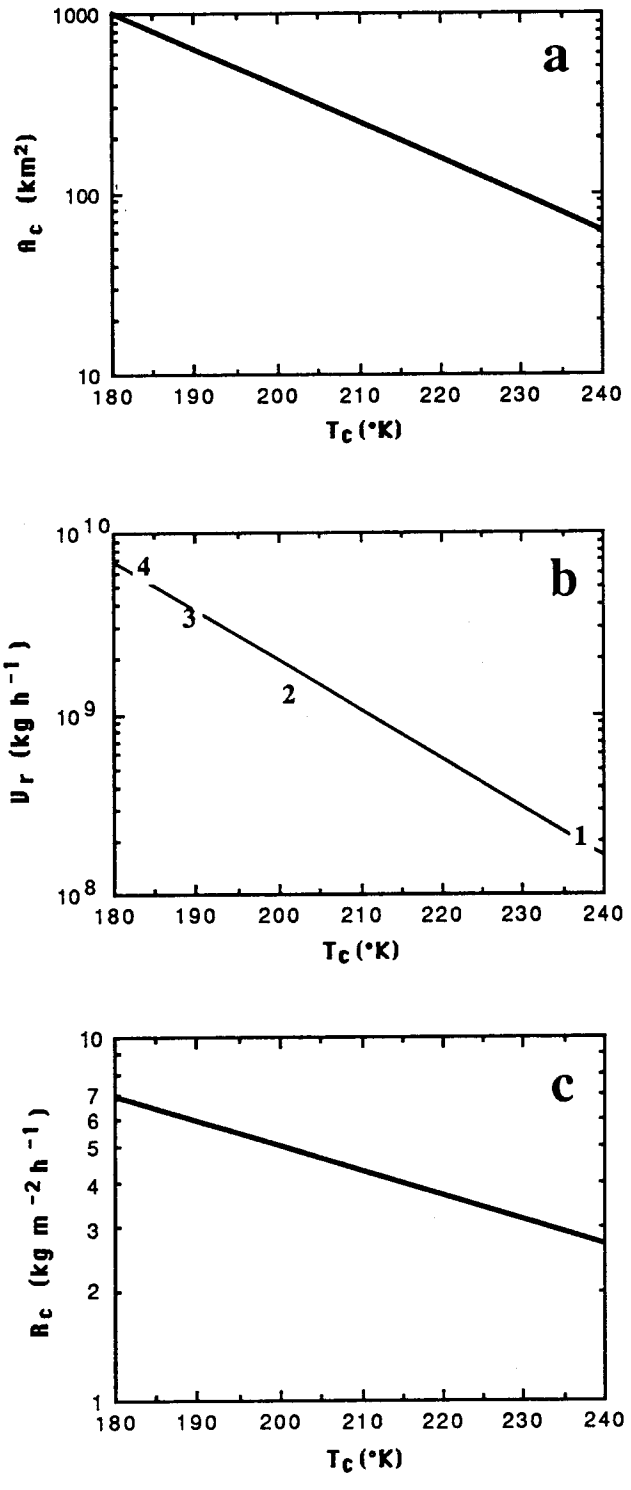


Fig. 5. Relationships for (a) areal coverage, $A_c$, (b) time rate of fallout of condensed water mass, $V_r$, and (c) mean rain rate, $R_c$, as functions of corrected cloud-top temperature, $T_c$, for convective cores as used in the CST cluster B application. Model updraft radii (in km) which resulted in $V_r(T_c)$ values shown in (b) are given by the plotted integers.

Table 1. Total area, $A_T$, and mean rain rate for convective precipitation for cluster B as determined by CH radar analysis and by CST applied to GMS-1 data. Radar results are taken from Fig. 19c in CH. CST results for this chart were tabulated only for region indicated by dashed line on Fig. 1. The mean rain rate is defined here as the average at all data points which have been determined by the radar technique or CST to be convective. The CST here employs (4) with AN parameters to determine convective area, and (10) to determine convective rate. Satellite data are not available for 0330 GMT and radar data are not available past 0330 GMT. The CST results shown in parentheses for 0330 are derived by linear interpolation between the 0233 GMT and 0533 GMT results.

| Time(GMT) | Total Convective Area ($10^3\times$ km$^2$) | | Mean Conv. Prec. Rate (kg m$^{-2}$ h$^{-1}$) | |
|---|---|---|---|---|
| 9–10 December | Radar (CH) | CST | Radar (CH) | CST |
| 1733 | 2.4 | 1.8 | 5.4 | 5.0 |
| 2033 | 5.9 | 6.6 | 4.8 | 6.2 |
| 2203 | 5.6 | 6.9 | 5.2 | 5.8 |
| 2233 | 5.2 | 7.6 | 6.0 | 5.5 |
| 2303 | 6.8 | 7.7 | 5.0 | 5.6 |
| 2333 | 6.3 | 7.1 | 4.1 | 5.4 |
| 0233 | 1.9 | 1.7 | 3.2 | 4.7 |
| 0330 | 1.2 | (1.5) | 5.8 | (4.5) |
| 0533 | — | 1.0 | — | 4.0 |

and 33.85 for $c$ and $d$, respectively, with a correlation of -0.986. Based on (4), (8), and (9), $R_{ci}$, in units of kg m$^{-2}$ h$^{-1}$ (*i.e.*, mm h$^{-1}$), can be given as

$$\ln(R_{ci}) = e\,T_{ci} + f, \tag{10}$$

where

$$e \equiv c - a = -0.0157, \tag{11}$$

and

$$f \equiv d - b = 4.76, \tag{12}$$

where $b$ has been adjusted to conform with units of m$^2$. This relationship for $R_{ci}$ is shown in Fig. 5c. Using (10), the value for $R_{ci}$ is assigned to the pixels comprising the convective precipitation area, as determined by (4), centered on each core. Rates for pixels located in overlapping convective areas are averaged.

The values of convective rain rate shown in Fig. 5c range from 3–7 kg m$^{-2}$ h$^{-1}$. These rates are in very good agreement with the values of 3–8 kg m$^{-2}$ h$^{-1}$ shown by Leary (1984) for convective cells 10–17 km in echo height in GATE cloud clusters (Leary 84, Figs. 10 and 11). Leary's values were smoothed over time and space in such a way as to be "suitable for comparison with and incorporation into satellite-derived estimates of rainfall because satellite data have a comparably coarse spatial and temporal resolution." The oceanic cloud clusters in GATE, moreover, had many apparent similarities to those observed in WMONEX, and therefore comparison to Leary's appears to be a reasonable test of the rates in Fig. 5c.

The mean convective precipitation rate $\overline{R_c}$ is shown in Table 1 several times for cluster B, where $\overline{R_c}$ is defined as the value of $R_{ci}$ averaged over all satellite pixels assigned a convective rain rate. The table compares $\overline{R_c}$ with the average rain rates from the radar rainfall estimates of CH for the same data times. The CST values for $\overline{R_c}$ are generally slightly higher than the average rain rate determined from the radar data. Area-weighted means of the average rain rates from Table 1 show that the CST rates are about 12 % higher overall. One of the possible reasons for the CST rates being higher than the radar rates is that the radar reflectivity data used in this comparison are from the 3 km level. It has been shown by Szoke *et al.* (1986) and Szoke and Zipser (1986), in their study of tropical convective cells in GATE, that it is typical to have an increase in the reflectivity from 3 km to the surface for convective cores. However, this effect is difficult to quantify, so for the purpose of this study, we accept the 12 % overall difference, which is as good an agreement as could be expected.

*e. Area covered by stratiform precipitation*

After the assignment of areas and rates to the selected convective cells, the next step is to identify the stratiform precipitation areas (see Fig. 2). To accomplish this, the CST chooses a stratiform threshold temperature, $T_s$, and designates all pixels in the image for which $T_b<T_s$ as stratiform, with the exception of those pixels previously designated as convective. The procedure to derive $T_s$ follows.

First, the mode of the temperatures ($T_{mode}$) in an 80 km by 80 km box, centered on each convective center for which $S\leq 4.0$, is determined. This cutoff value of $S$ was selected empirically by AN to exclude the young, growing convective cells which normally have larger slopes than the mature systems with ex-

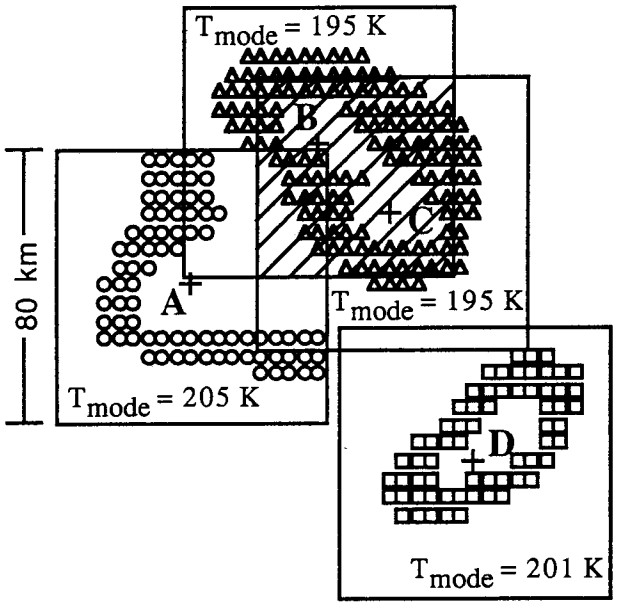


Fig. 6. Example of modal grid used for $T_s$ calculations. Crosses (A, B, C, and D) indicate four convective centers for which $S \leq 4.0$. The box enclosing each center shows the area (80 km by 80 km) over which the $T_{mode}$ for that core is measured. The other symbols show the locations of all pixels in each box for which $T_b = T_{mode}$. The circles, triangles and squares represent pixels for which $T_b$ equals 205°K ($T_{mode}$ for center A), 195°K ($T_{mode}$ for centers B and C) and 201°K ($T_{mode}$ for center D), respectively. In the east-west direction, the data are shown only for every other pixel. The shaded region is the intersection of the boxes for centers B and C.

tensive cirriform anvils. Pixels with $T_b \geq 253$ K are not included in the $T_{mode}$ calculations in order to eliminate effects of the earth's surface. The modal temperature is intended to be an approximation to the IR temperature associated with the "flat", near-tropopause portion of the mesoscale anvils associated with the convective cores and has been shown by Adler *et al.* (1985) to be well correlated with the near-tropopause neutral-point temperature.

Figure 6 gives a hypothetical example of a group of four convective cores used in calculating $T_s$. The symbols in the 80 km by 80 km box around each core show the positions of all of the pixels in that particular box for which $T_b = T_{mode}$. AN set $T_s$ equal to the weighted mean of all of the modal temperatures for that image:

$$\overline{T_{mode}} = \frac{\sum_i W_i T_{mode_{(i)}}}{\sum_i W_i}, \tag{13}$$

where $T_{mode_{(i)}}$ is the mode temperature for the $i$-th convective cell and $W_i$ the number of pixels in the box surrounding that cell for which $T_b = T_{mode_{(i)}}$.

We have made two refinements to the method used by AN to determine $T_s$. First, we have modified the method for calculating $\overline{T_{mode}}$ in order to remove a bias that their method has towards the $T_{mode}$ for a cluster of cores. This bias problem is illustrated in the group of cells shown in Fig. 6. Note that if (13) is used to calculate $\overline{T_{mode}}$, then all of the pixels within the shaded region (the intersection between the boxes for cores B and C) are counted twice. It is not unusual, especially in intense convective areas with very cold cloud tops, for there to be a great deal of overlap for regions having the same $T_{mode}$. Of course, overlaps have no impact if each of the overlapping regions have a different $T_{mode}$ as in the case shown in Fig. 6 where the A or D boxes overlap with either the B or C boxes. The bias problem is alleviated in this study by not counting any pixel more than once in the $\overline{T_{mode}}$ computation. This is accomplished by creating a "modal grid" for each image consisting of all pixels for which $T_b$ equals the $T_{mode}$ of any of the boxes within where a pixel is located. In the example given in Fig. 6, the union of all of the pixels shown in the figure would constitute the modal grid. The modified $T_{mode}$ is equal to the mean of the modal grid given by

$$\overline{T_{mode}} = \frac{1}{n} \sum_{j=1}^{n} T_{b_{(j)}}, \tag{14}$$

where $n$ is the number of pixels in the modal grid, and $T_{b_{(j)}}$ is the IR temperature of the $j$-th pixel on that grid. For the example given in Fig. 6, $\overline{T_{mode}} = 198$°K using (13) and 199°K using (14).

The second change we have made in the assignment of $T_s$ is to use

$$T_s(^\circ K) = \overline{T_{mode}} + x, \tag{15}$$

where $x = 7$°K, rather than $T_s = \overline{T_{mode}}$. This modification appears to be necessitated by the criteria AN used to determine the extent of the stratiform precipitation region from the radar data versus the method used by CH. In their analysis of Miami radar data for their Florida study, AN excluded all echoes <25 dBZ (*i.e.*, $<1\,\mathrm{kg\,m^{-2}\,h^{-1}}$), whereas CH included all echoes ≥1 dBZ. The need for the addition of 7°K to $\overline{T_{mode}}$ is illustrated by the following figures. Figure 7 shows the convective and stratiform rain structure for cluster B from the CH radar analysis for 2221 GMT on 9 December. Figures 8a, 9a, and 10a show CST-derived convective and stratiform rainfall patterns for the three satellite times, 2203, 2233 and 2303 GMT, respectively, nearest the time of the CH radar analysis, for $T_s = \overline{T_{mode}}$. Note that, for reasons discussed in Sec. 2, only the region within the dashed line has been used in the comparisons of the CST results and the CH radar analysis

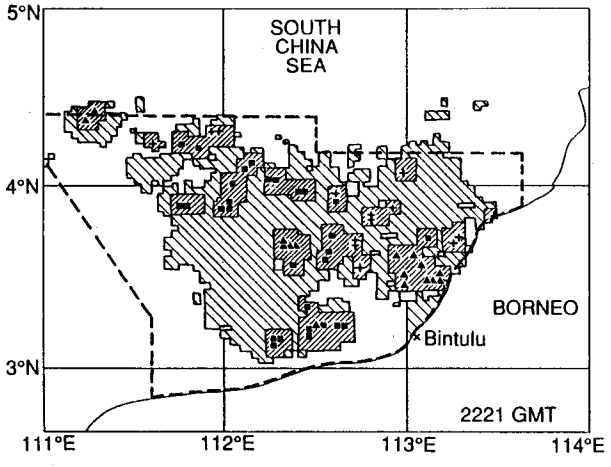


Fig. 7. Radar-echo patterns at 3 km in cluster B at 2221 GMT on 9 December 1978. Light-and dark-shaded regions indicate stratiform and convective precipitation, respectively. The dBZ values of objectively identified convective cores are indicated by crosses (21–30 dBZ), squares (31–40 dBZ) and triangles (>40 dBZ). Adapted from Churchill and Houze (1984a). The outer map boundary and dashed line correspond to the dotted and dashed lines in Fig. 1, respectively.

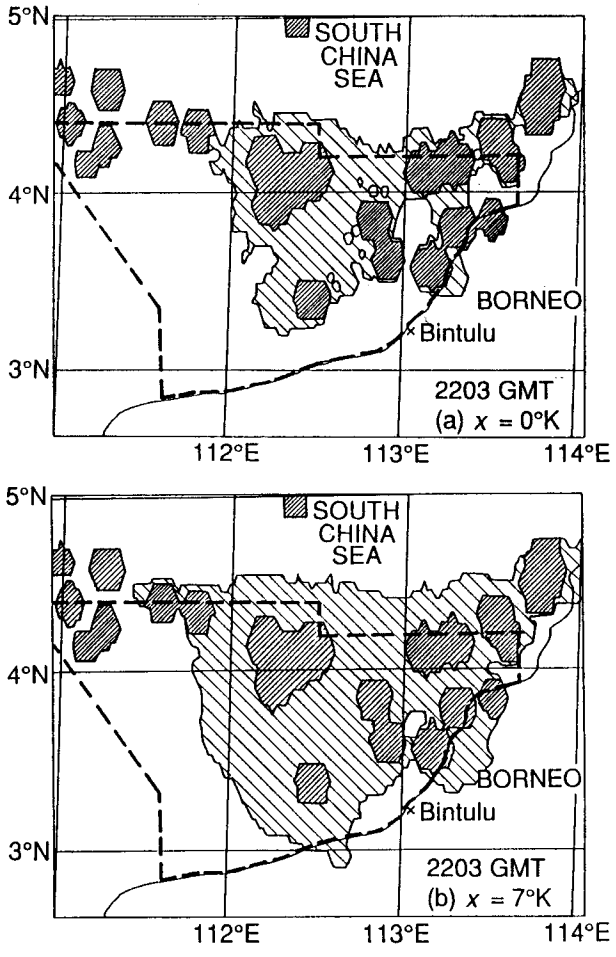


Fig. 8. CST-derived rainfall regions using GMS-1 IR data for cluster B at 2203 GMT on 9 December 1978. Light-and dark-shaded regions indicate stratiform and convective precipitation, respectively. The stratiform regions are shown for $T_s=\overline{T_{mode}}+x$, where $x$=(a) 0°K and (b) 7°K. The convective regions were assigned according to (4) using parameters from AN. The region over which the CST results are tabulated in Secs. 3 and 4 is outlined by the dashed line (as in Fig. 1). The shapes of the convective areas are the result of the algorithm used to assign the area around each convective core.

results. The regions closest to the radar, but within the dashed line, were given the greatest consideration in the comparisons referred to here. It can be seen from comparing Figs. 8a, 9a and 10a with Fig. 7, that the use of $T_s=\overline{T_{mode}}$ underestimated the areal extent of the stratiform regions as pictured in the CH radar analysis. By letting $T_s=\overline{T_{mode}}+x$, with $x$=7°K (see Figs. 8b, 9b and 10b), the CST produced larger stratiform regions that are in better agreement with the radar analyses of CH. The choice of 7°K for $x$ in (15) was made by a qualitative comparison of the stratiform regions based on $T_s=\overline{T_{mode}}+x$, where $x$ ranged from 0 to 9°K for the eight satellite times from 1733 to 0533 GMT on 9–10 December, with the radar-derived patterns from CH.[3] The value for $x$ that resulted in the best match, on the average, between the CST- and radar-derived stratiform precipitation patterns for all eight image times was 7°K.

The choice of $x$=7°K is also supported by Fig. 11. This figure compares the CST-derived stratiform precipitation areas as determined by $T_s=\overline{T_{mode}}+x$, for $x$=0, 3, 5, 7, and 9°K, where $\overline{T_{mode}}$ is calculated using (14), with the CH radar-derived stratiform precipitation areas for 1733 to 0330 GMT[4] on 9–10 December, which is the period the radar-detected rainfall from cluster B was observed (CH). For the case $x$=0, *i.e.*, $T_s=\overline{T_{mode}}$, the CST-derived stratiform region is too small for most image times by at least 50 percent. Although the closest overall satellite-radar match in Fig. 11 is for $x$=5°K, the qualitative comparisons discussed above revealed that $x$=7°K showed closer agreement in the south-

[3]Radar-echo patterns for intermediate times not included in CH were also used in the comparisons.

[4]The last time included in the CH analysis is 0330 GMT on 10 December. Comparisons between the CST and CH results at that time are based on linear interpolation between the 0233 and 0533 GMT satellite observation times.

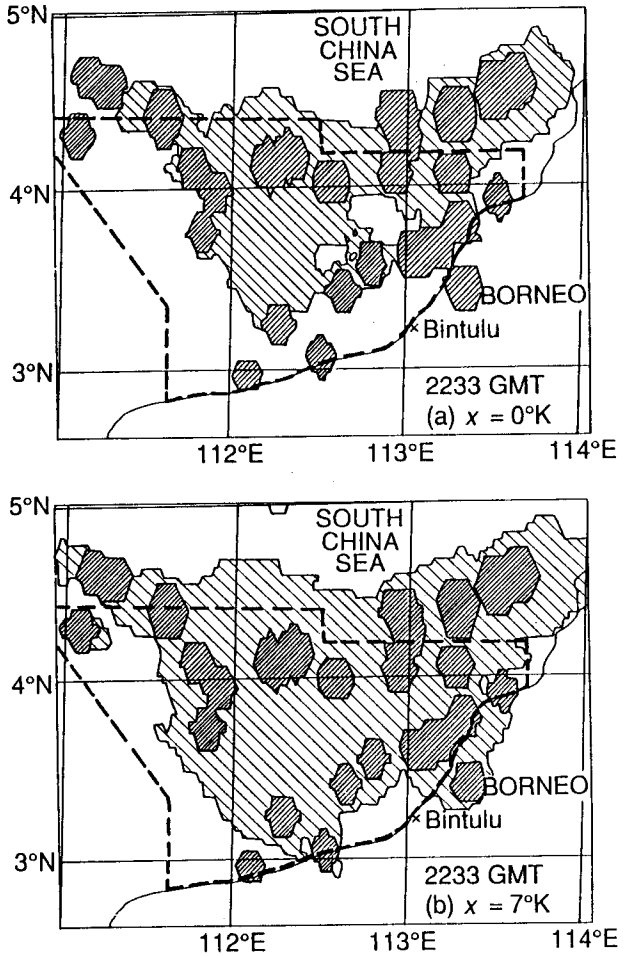


Fig. 9. Same as Fig. 8, except for 2233 GMT.

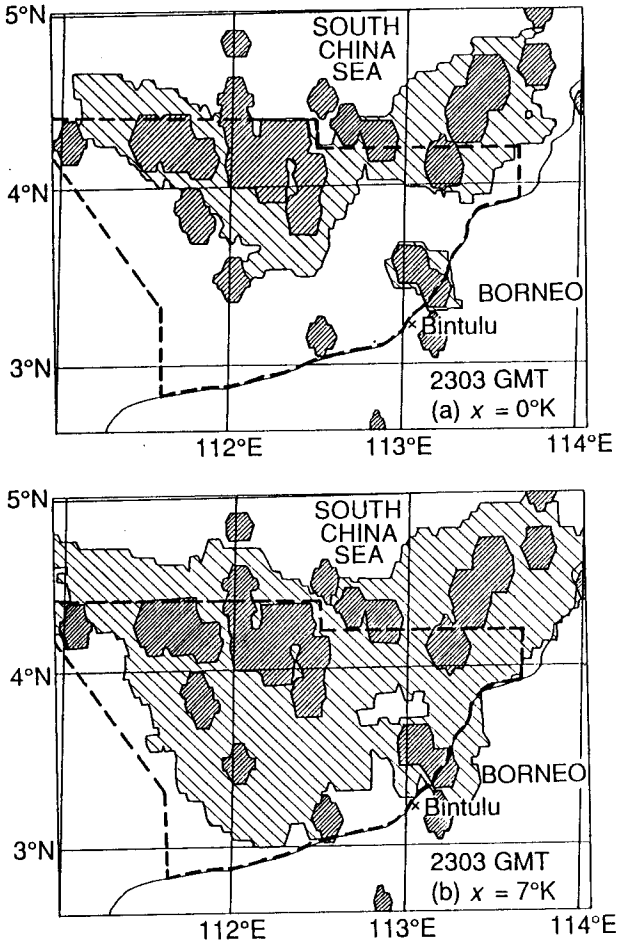


Fig. 10. Same as Fig. 8, except for 2303 GMT.

ern portions of the radar coverage, where the quality of the radar data was most reliable because of their closer proximity to the radar site. This qualitative agreement in the southern part of the region was especially evident after 2233 GMT, which coincides with the period during which the $x$=5°K and $x$=7°K plots (Fig. 11) have the greatest disagreement. As explained earlier, it would be expected that the CST-derived areas, if "correct", should almost always be equal to or greater than the radar-derived areas, but never less. The $x$=7°K line shows a larger difference from the radar line as the cluster extended to the northwest and moved further from the location of the radar. For our application, we conclude that the stratiform regions can be adequately determined through the use of the above procedure, *i.e.*, (14) and (15), where $x$=7°K.

*f. Assignment of stratiform rain rate*

The next step in applying the CST (see Fig. 2) is to assign rain rates to the stratiform regions bounded by $T_s$. The method used by AN was to assign a nominal rain rate of $2\,\mathrm{kg\,m^{-2}\,h^{-1}}$ (*i.e.*, 2 $\mathrm{mm\,h^{-1}}$) to the pixels classified by the technique as stratiform. In a very thorough and careful analysis of rain rates in GATE cloud clusters, Leary (1984) also found $2\,\mathrm{kg\,m^{-2}\,h^{-1}}$ to be the typical rain rate in the stratiform regions. The mean stratiform rain rate, $\overline{R_s}$, determined by the CH radar analysis for cluster B, is shown in Fig. 12, along with the stratiform threshold temperature ($T_s$) determined by (14) and (15), and the average convective cell temperature, $\overline{T_c}$. These data show that the $\overline{R_s}$ increased steadily from 1 to $3.5\,\mathrm{kg\,m^{-2}\,h^{-1}}$ between 1733 and about 0330 GMT, after which the rain area was out of radar range. However, during this time period, the overall (area-weighted) mean of $\overline{R_s}$ is almost exactly $2\,\mathrm{kg\,m^{-2}\,h^{-1}}$. The trend of $\overline{R_s}$ after the cluster's rain area was out of radar range is not known. However, the rate would be expected to decrease, as the anvil cloud became thinner and less productive and as sub-cloud-base evaporation became more prominent with the probable rising of the cloud base during the dissipation period. Since $T_s$ and $\overline{T_c}$ were increasing strongly at 0330 when the radar information ended, general weakening of the convection and thinning of the cirrostratus is indicated, suggesting that dissipation and hence lower $\overline{R_s}$ would ensue after this time. In view of these observations, as well as the results of Leary (1984), it seems reasonable to

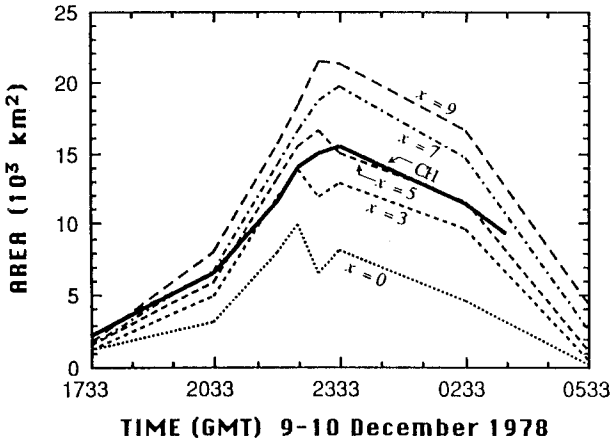


Fig. 11. Area covered by stratiform precipitation as determined by CST application (dashed and/or dotted lines) and CH radar analysis (darker solid line) for cluster B. CH results are interpolated from Fig. 19c in CH to match GMS-1 image times. CST results are plotted for $T_s=\overline{T_{mode}}+x$, where $x$=0, 3, 5, 7, and 9°K. CST results only include data located within region indicated by dashed line in Fig. 1.

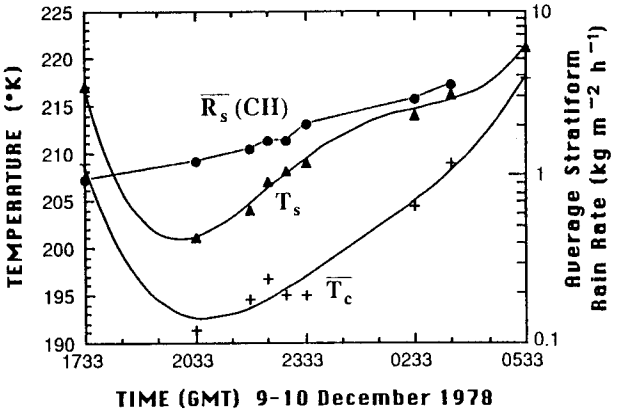


Fig. 12. Average of corrected cloud-top temperatures ($\overline{T_c}$) for convective cores selected by CST (within dashed region in Fig. 1), and CST-determined values of stratiform threshold temperature ($T_s$) as determined by (14) and (15), for twelve hours during the life cycle of cluster B. The solid curves show smoothed functions of time (given here nominally by 4th-order polynomial fits) for $T_s$ and $\overline{T_c}$. Also included are radar-determined values (from CH) for the average stratiform rain rate ($\overline{R_s}$), given on a logarithmic scale.

adopt the average rate of 2 kg m$^{-2}$ h$^{-1}$ assumed by AN for our calculations throughout the cluster's life cycle. We have also carried out calculations using 1 and 3 kg m$^{-2}$ h$^{-1}$, which are probably reasonable lower and upper limits for the stratiform rate.

## 4. Results of application of the modified CST to the portion of cloud cluster B covered by ground-based radar

The results for the application of the modified CST, described in Sec. 3 and outlined in Fig. 2, to the region enclosed by the dashed line in Fig. 1, are presented in Figs. 13 through 15. These figures compare the CST- and radar-derived precipitation areas, area-integrated rain rates, and time-integrated results in the limited region for which reliable radar data were available for cluster B. The subdivision of the radar data into convective and stratiform components follows CH.

Figure 13a shows the convective, stratiform, and total (sum of convective and stratiform) precipitation areas for the radar and satellite analyses. Figure 13b shows the percent contribution to the total precipitation area from the convective and stratiform components. The CST curves in Fig. 13a display a general agreement with the CH radar results. As discussed in Secs. 3c and e, the CST-derived areas are somewhat larger than the radar values for most of the later data times possibly due to attenuation and beam-blockage problems that affect the radar but not the satellite data. The satellite analysis shows the total precipitation area growing from $3.2\times10^3$ km$^2$ at 1733 GMT, to a maximum of $27\times10^3$ km$^2$ at 2333 GMT, and decreasing again as the convection dissipated and the cluster moved out of the analysis region.

Figure 13b shows excellent agreement in the percentage contributions of the areas covered by convective and stratiform rainfall to the total area from the radar and satellite analyses. The radar and satellite values are within five percent of each other for all data times. Both methods show the fractional area covered by the stratiform precipitation increasing from a minimum of ~45 % at 1733 GMT on 9 December to a maximum of ~90 % at 0233-0330 GMT on 10 December. Thus, even if the CST is slightly overestimating or underestimating the absolute areas covered by precipitation, the relative sizes of the convective and stratiform areas conform well with radar results.

Figure 14a shows the convective, stratiform and total area-integrated rain rates for the radar and satellite analyses. Figure 14b shows the percent contribution to the total area-integrated rain rates from the convective and stratiform components. As with the results for the area given in Fig. 13a, the CST curves in Fig. 14a display a general agreement with the CH radar results. The main difference between the CST curves and curves for the CH radar results for the total and stratiform area-integrated rain rates is due to the choice of a constant value (2 kg m$^{-2}$ h$^{-1}$) for the stratiform rate used by the

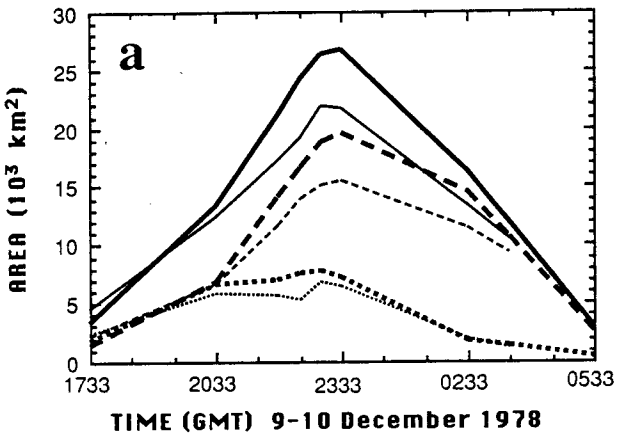


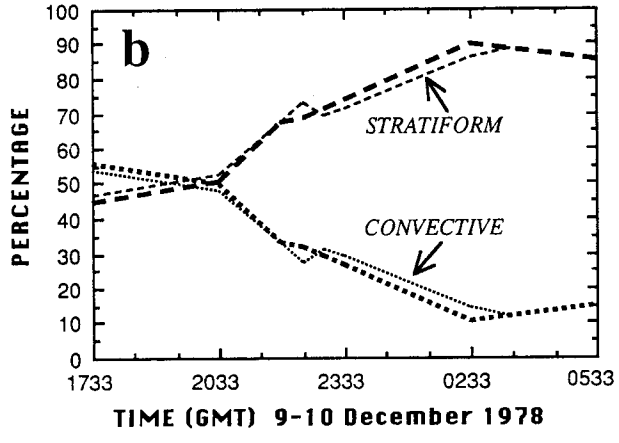


Fig. 13. (a) Convective (short-dash lines), stratiform (long-dash lines) and total (sum of convective and stratiform: solid lines) precipitation areas as determined by application of modified CST (darker lines) and CH radar analysis (lighter lines) to cluster B. CH results are interpolated from Fig. 19c in CH to match GMS-1 image times. Only data located within the region indicated by the dashed line in Fig. 1 are used in the CST results. (b) Percent contributions to total rainfall area by convective (short-dash lines) and stratiform (long-dash lines) precipitation regions for CST (darker lines) and radar (lighter lines) results.

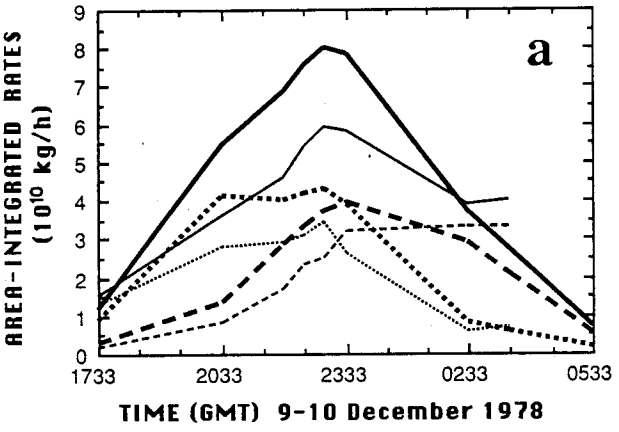


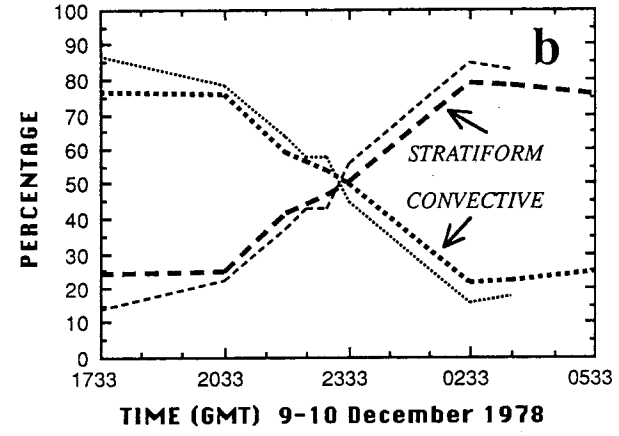


Fig. 14. (a) and (b) are as in Figs. 13a and b, respectively, except for area-integrated rain rates.

CST (discussed in Sec. 3f). With the curves for area shown in Figs. 13a and b being in fairly good agreement between the CST and radar results, it is anticipated that the CST-derived stratiform (and therefore the total) area-integrated rain rates would be too high or too low when the radar-observed values for $\overline{R_s}$ are less than (before 2333 GMT) or greater than (after 2333 GMT) 2 kg m$^{-2}$ h$^{-1}$, respectively. However, these differences average out over the time period discussed in this section, since the average radar-observed value for $\overline{R_s}$ is very close to 2 kg m$^{-2}$ h$^{-1}$.

The CST again appears to perform better in the determination of the relative contributions than the absolute amounts from the convective and stratiform components. Figure 14b shows fairly good agreement in the percentage contributions of the convective and stratiform area-integrated rain rates from the radar and satellite analyses, with the main shortcoming again being the difference between the stratiform rates discussed above. The CST results show the stratiform contribution increasing from a minimum of 24 % at 1733 GMT on 9 December to a maximum of 78 % at 0233 GMT on 10 December.

Figure 15a and b show the areal coverage and area-integrated rain rates, from Figs. 13a and 14a, respectively, integrated over ten hours of the cluster B lifetime, 1733 GMT through 0333 GMT on 9–10 December. These time-integrated values for the convective and stratiform contributions show the same tendencies as mentioned above in the discussion about Figs. 13 and 14. The absolute amounts for the CST-derived data given in Fig. 15 are higher than

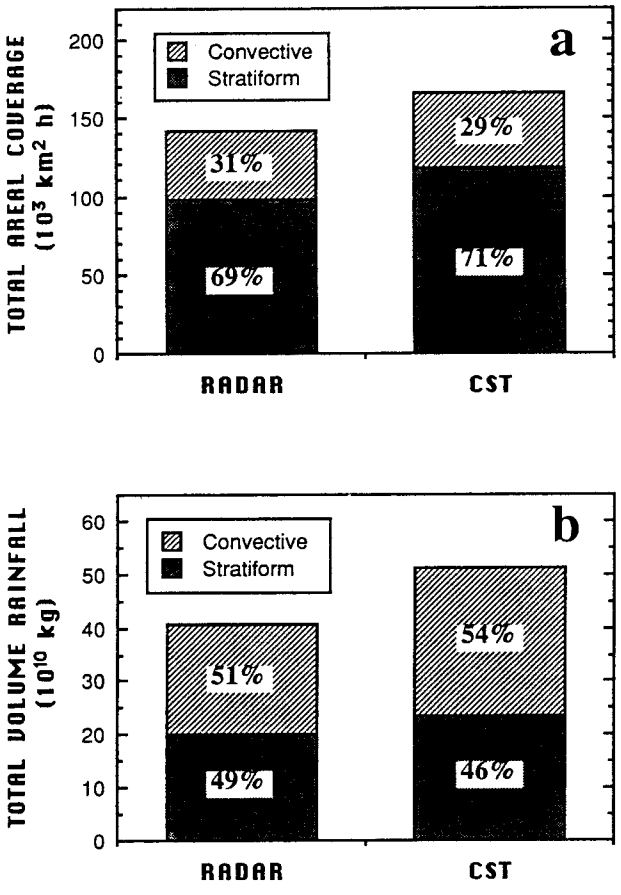


Fig. 15. Stacked column graphs for time-integrated radar- and CST-derived (a) areal coverage of rainfall (from Fig. 13a) and (b) area-integrated rain rates (from Fig. 14a). Data are from 1733 GMT through 0333 GMT, 9–10 December. Convective and stratiform contributions to time-integrated amounts are represented by hatched and shaded regions, respectively. Percentage contributions of the two components to the total amounts are also shown.

the radar-derived data by about 20 %. However, the relative amounts of convective and stratiform contributions in both Figs. 15a and b are within a few percent for the radar and CST results.

## 5. Application of modified CST to all of cluster B

*a. Extension of the limited-area analysis*

The general agreement between the satellite CST results and the radar analysis of CH over the limited region considered in Sec. 4 lends confidence to the further application of the CST to cloud cluster B over the complete period of its life history, beyond the area and time period of the WMONEX radar data analyzed by CH.[5] To assure that the modified CST faithfully represents the convective-stratiform structure of cluster B, the quantitative comparisons in Sec. 4 deals only with the portion of the cloud shield that intersected the area covered by the WMONEX radar at Bintulu and with the time period limited to that covered by the CH analysis of the radar data. To present a complete history of the convective and stratiform components of the cluster, the present section extends the modified CST developed in Sec. 3 for the limited area to the entire areal extent of cluster B and over its full lifetime.

This analysis begins at 1733 GMT on 9 December, the same time as the start of the partial analysis, but extends through 1133 GMT on 10 December. These are the first and last satellite image times, respectively, in which cluster B can be identified (CH). The spatial domain for each individual satellite time used in this application of the CST consists of the box enclosing all cloud elements associated with the cluster at that particular time (as indicated in Fig. 6 of CH). Figure 1 shows the composite of the cirrus cloud shield (shaded region) associated with cluster B during its lifetime, an area of over $220\times10^3$ km$^2$. We have defined the cirrus shield area for each image as the sum of the areas of all pixels in the satellite IR imagery within the box described above for which $T_b$ is less than or equal to some cloud-top threshold temperature. We have chosen 245°K for the threshold temperature, which is rounded off from the value of 244.5°K used by CH to define the cluster B cirrus shield. CH chose their value as a result of subjective examination of the GMS-1 visible and IR imagery. Also shown in Fig. 1 is the spatial coverage for the partial analysis presented in the previous sections. The size of the fixed, limited analysis area is $37\times10^3$ km$^2$, or only about 16 % of the cumulative region covered by the cloud shield.

The larger spatial domain used for the complete analysis suggests that the calculations for the threshold temperature, $T_s$, would be affected by the inclusion of a larger number of convective cores around which the $T_{mode}$ values are computed (see Sec. 3e). Figure 16 compares $T_s$ values for the partial and complete cluster B analyses. All of the values for $T_s$ from the two analyses are within 1°K except for 1733 and 2033 GMT. The difference at 1733 GMT results from the inclusion of a separate (at that time) portion of cluster B to the northeast of the limited analysis area. At that time, $T_s$ for the complete analysis is a weighted average of the $T_s$ values for the two clusters. Although this means that the resulting $T_s$ is not representative for each cluster separately, the errors should tend to cancel when calculating the total stratiform rain area for that particular image. By 2033 GMT, the two clus-

[5]The overall history of cluster B can be reviewed in the sequence of satellite images of the cloud shield shown in Fig. 6 of CH.

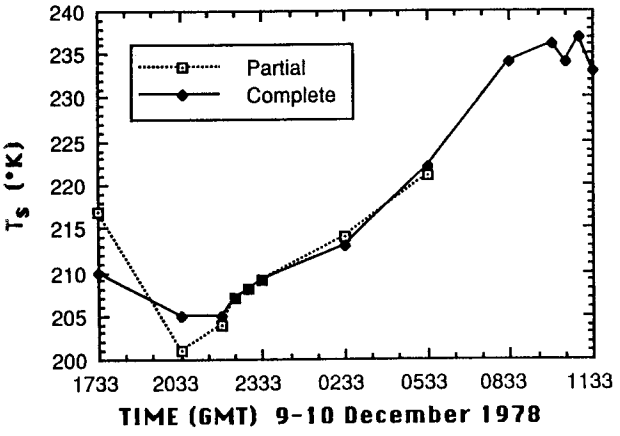


Fig. 16. $T_s$ for partial (dotted line) and complete (solid line) cluster B CST analyses.

ters had merged. However, the northeast section, still outside of the domain of the partial analysis, retained characteristics that were different enough to alter $T_s$ for the complete cluster.

*b. Verification of the location of satellite-inferred convective and stratiform precipitation areas with ship and aircraft observations*

Although cluster B moved out of range of the coastal radar during its later stages, it moved over the location of one of the research ships and was sampled by the two research aircraft. The data obtained by the ship and aircraft allow the satellite-inferred locations of the convective and stratiform regions to be verified at the locations of these observations. Consistency with these additional "ground-truth" data lends further confidence to the application of the CST to the entire cloud cluster B.

The Soviet ship *Ak. Korolov* (location shown in Fig. 1) was in the general proximity of cluster B during most of the cluster's lifetime. As the P3 and Electra research aircraft flew in the vicinity of cluster B, they deployed Omega dropwindsondes (ODWs: Julian 1982) at selected points along the flight track to determine vertical profiles of temperature, humidity and horizontal wind. On board the P3, quantitative radar reflectivity data were obtained with a lower fuselage C-band weather radar, as described in CH. In addition, scientists aboard the two aircraft recorded various visual observations and impressions. Visual and photographic observations of clouds from aboard the aircraft have been described and analyzed by Warner (1982).

As in the comparisons of the CST results with the ground-based radar data, uncertainties in the precise location of the satellite data can affect the comparisons with the ship and aircraft data. In addition, as will be discussed below, the satellite times frequently do not coincide with the ship or aircraft observation times. These shortcomings are important to keep in mind in consideration of the high degree of variability of the cluster's precipitation structure in space and time.

The current weather reports by the ship *Ak. Korolov* during the passage of cluster B are shown in Fig. 17. Also shown are results from the complete CST analysis of cluster B and the cirrus cloud shield boundaries for the region immediately surrounding the ship. The CST results are shown for 2033 GMT on 9 December through 1033 GMT on 10 December; the time period during which precipitation associated with cluster B (according to CST results or ship observations) was located near the ship. Ship reports are given on the hour, while CST results (at satellite observation times) are approximately on the hour or half hour. The closest ship observation time(s) are used in the comparisons with the CST results discussed here.

The ship observations agree very well with the CST-derived precipitation patterns. The ship's first observations of the convective cells associated with the cluster took place at 2000 and 2100 GMT, when they reported lightning in the distance. At 2033 GMT, about halfway between these two ship observation times, the CST analysis shows the closest convective cells at about 35–50 km from the ship. Then, from 2200 GMT on the 9th through 0100 GMT on the 10th, the ship recorded observations of rainfall reaching the surface, but not at the ship's location. During this time period, the CST analysis shows convective and stratiform precipitation near, but not at the ship's location. The ship only recorded precipitation (from moderate and light showers) from 0200 through sometime between 0500 and 0600 GMT. During this time period they measured approximately 6 mm of rainfall. The CST results for 0233 and 0533 GMT both show precipitation over the ship's location. The ship was near the border of stratiform and convective regions delineated by the CST. The reported amount at the ship is consistent with this result. At the next two satellite observation times, 0833 and 1003 GMT, the CST results show stratiform precipitation from cluster B from about 15–30 km from the ship, mainly to the northwest. Additional precipitation is shown to the east, but at a distance of at least 50 km from the ship. These results agree with the ship observations from 0700 GMT through 1000 GMT, when the ship again reported observing precipitation reaching the ground, but not at the ship's location. Finally, the 1033 GMT CST analysis shows no precipitation within 70 km of the ship, while the dissipating remnants of cluster B moved off towards the northwest. The 1100 GMT (and subsequent) ship reports reflected this with reports of "dissolving clouds."

Rawinsonde data from the *Ak. Korolov* (not shown here) were discussed thoroughly in CH. The sounding at 0000 GMT, two hours before the pre-

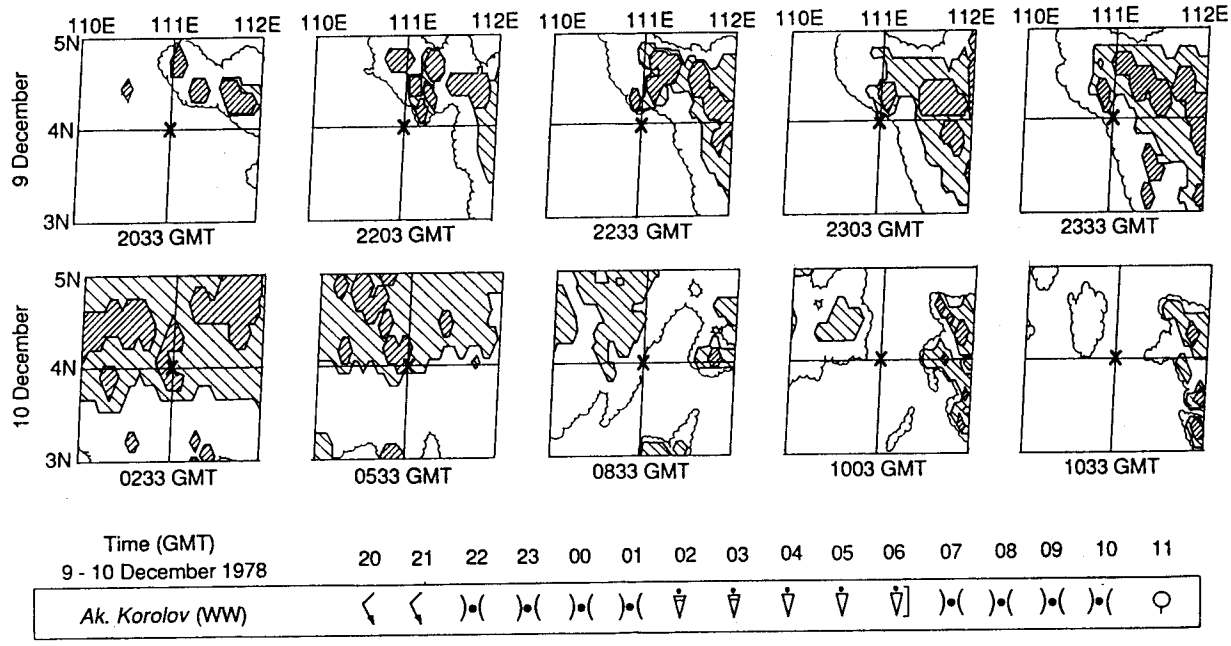


Fig. 17. Time series of CST-derived rainfall regions from the complete cluster B analysis for the 2° latitude by 2° longitude box centered on the location (indicated by X) of the Soviet ship *Ak. Korolov*. Light- and dark-shaded regions indicate stratiform and convective precipitation, respectively. The perimeters of the cirrus shield (as defined by 245°K threshold) are indicated by scalloped lines. Also shown are the current weather observations (WW) from the ship.

cipitation associated with the cluster moved over the ship, was very similar to the mean WMONEX sounding (shown in CH). Later *Ak. Korolov* soundings shown in CH, for 0800 and 0900 GMT, depict the presence of the stratiform cloud deck, evidence of a mesoscale unsaturated downdraft below the cloud, and a low-level subsidence inversion. These later soundings are consistent with being taken from underneath the stratiform cloud shield but outside the area of rain reaching the surface (Zipser, 1977). At the time of these two later soundings, the ship was under the fringe of the cluster's cirrus shield, outside of the CST-indicated rain area (see Fig. 17).

The flight track of the Electra along with the CST results for the closest satellite time (0833 GMT on the 10th) are shown in Fig. 18a. The previous satellite data time was three hours earlier at 0533 GMT. Thus, the earlier parts of the flight path that intersected cluster B differ from the closest satellite time by as much as 45 min. Because of these time differences and possible satellite-data location errors, comparisons can only be made with the CST results for the general region in the vicinity of the aircraft path.

Observers on board the Electra frequently reported towering cumulus and noted regions of fully developed convective cells, which the aircraft occasionally penetrated. These observations are consistent with the analysis of Warner (1982), who also noted "individual cumulonimbi" beneath the "thick cirrus" anvil of the cloud cluster (see Warner 82, Fig. 16a). As discussed by Warner (1982) and by Johnson and Houze (1987, their Sec. 2.3), it was typical in WMONEX for convective clouds of increasing height to be seen over the ocean as the aircraft approached and entered the region of a cloud cluster (*e.g.*, Fig. 11 of CH). Probably only a select few of these convective towers produced large amounts of rain and penetrated the cirrus shield so that they would be detected by the CST. This helps to explain why more sightings of cumuliform shapes appeared in the observers' logs than were evident in the CST patterns.

Much of the Electra's flight in the vicinity of cluster B at an altitude of ~6.4 km was near the base of an altostratus cloud deck, forming as a result of the convection. Warner (1982) noted that the base of this stratiform cloud shield was sloped. At 0744 GMT, observers reported towering cumulus building and forming the altostratus layer as the aircraft entered the region that comprises the precipitation region in the 0833 GMT CST analysis (see Fig. 18a). It is possible that the aircraft observed no precipitation at this time because the cluster was just forming in that region. This inference is supported by the CST analysis for 0533 GMT (not shown), which shows the area of precipitation associated with cluster B at that earlier time still lying to the south of the 0744 GMT aircraft position.

The next aircraft observation (0745 GMT) of a dry-air region with suppressed convection to the left of track (but still with convection to the right of

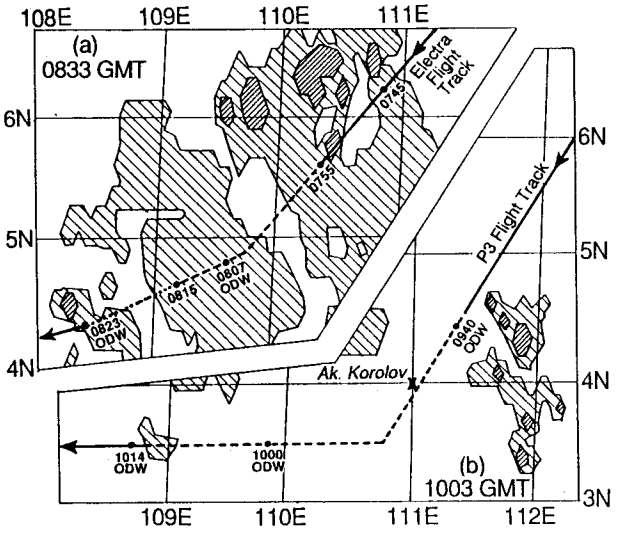


Fig. 18. Portions of the (a) Electra and (b) P3 flight tracks in the vicinity of cloud cluster B on 10 December 1978. Dashed and dotted sections of flight tracks indicate where the aircraft were in cloud and in precipitation, respectively. Also shown are CST-derived rainfall regions from the complete cluster B analysis for (a) 0833 GMT and (b) 1003 GMT for the regions surrounding the flight paths. Light-and dark-shaded regions indicate stratiform and convective precipitation, respectively.

track) roughly coincides with the locations in the CST analysis for 0833 GMT of the CST-derived hole in the precipitation, to the left and right of track, and the convective cells to the right of track. At 0755 GMT, the aircraft entered the altostratus cloud deck and remained in it until ~0815 GMT. No convection was encountered in the cloud. From about the time that the Electra came out of the altostratus cloud deck, until ~0823 GMT, light and heavy stratiform precipitation were noted, except for the brief period when they were in cloud again (see Fig. 18a). It is reasonable to conclude from these observations, that most of the track from 0755 until 0823 GMT probably passed through a region of stratiform precipitation, as indicated by the CST analysis. It cannot be determined from the aircraft scientists' observations whether there was precipitation taking place during the time when the aircraft was in cloud. The sounding from the ODW at 0807 GMT, the time the Electra was in cloud, and the ODW sounding at 0823 GMT, when the Electra was at the edge of the observed stratiform precipitation region, are shown in Figs. 19a and 19b, respectively. Both soundings show circumstantial evidence of a mesoscale downdraft of the type indicated by the ship observations and discussed by CH. That is, they both have, to some degree, the "onion shape" discussed by Zipser

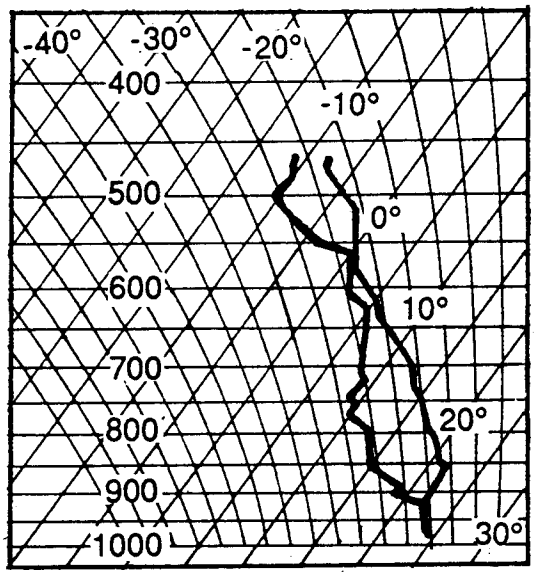


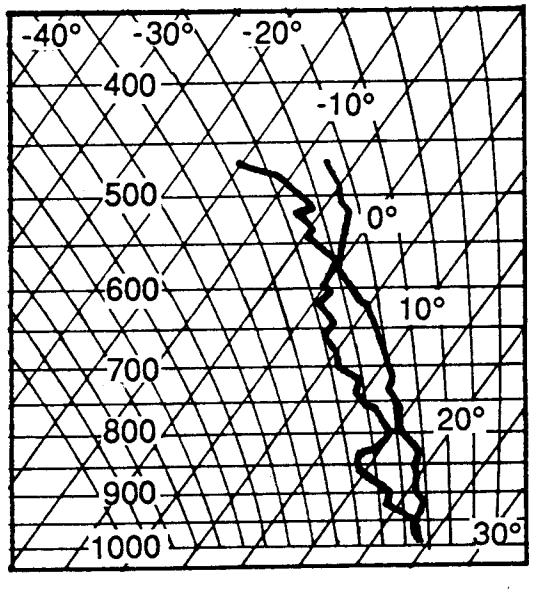


Fig. 19. Electra ODW soundings for (a) 0807 GMT 10 December 1978, released at 4.80°N, 109.66°E, and (b) 0823 GMT, released at 4.30°N, 108.44°E. Solid curves show temperature and dew point.

(1977); they contain layers characteristic of subsidence and drying located between a saturated region found at the melting level and a moist mixed layer near the surface. Thus these soundings, as well as the ship soundings discussed in CH, are consistent with a location within a stratiform precipitation region. However, it is not possible to determine from these soundings how much of the precipitation evaporated before reaching the sea surface.

Figure 18b shows a portion of the 10 December flight track of the P3, which flew at an altitude close to 7.8 km. The data overlaid on the P3 flight track are CST results for 1003 GMT. The feature located to the left of track near the 0940 GMT aircraft position was actually not a portion of cluster B. This feature does not appear in the reflectivity data from the P3 lower fuselage radar prior to the gap in the radar data that occurred from 0940–0949 GMT. It is not clear whether this feature was a cell identified spuriously by the CST or whether it was too small or weak to be identified by radar. Another possible explanation for the absence of the feature in the radar data can be the time difference between the aircraft and satellite data (over 20 min at the point in the flight track just prior to the data gap), combined with possible location errors in the satellite data. Although the feature was present in the CST analysis for the previous satellite time, 0833 GMT; it was even weaker, and the CST-determined convective cells were located at least 70 km from the aircraft. This small feature is the only irreconcilable difference that we have found between the CST and aircraft or ship data. According to the CST results, the convective cores in that region are very weak, and, even if they were real, might not have been measured by the aircraft radar due to the large vertical beam width. (Problems associated with the large vertical beam width were described by Houze *et al.*, 1981a.)

After the gap in the radar data, as mentioned in CH, the radar did detect very light echoes immediately surrounding the aircraft from 0950-0956 GMT, at the time of its flight-over the ship *Ak. Korolov.* But, as shown by the ship observations (see Fig. 17), none of this precipitation was observed to reach the ground at the ship's location, in agreement with the CST results, which indicate no precipitation over the flight track at this time. The next skip in radar data occurred from 0956-1014 GMT, so no observations were made to verify specifically the very small CST-derived region of stratiform precipitation shown near the P3 position just prior to 1014 GMT. According to the CST analysis, this was the only precipitation area from cluster B actually intercepted by the P3 aircraft. By the next CST time, 1033 GMT, this small patch had almost totally dissipated. The existence of this small patch is indicative that the stratiform cloud shield in the vicinity of the flight track was just marginally nonprecipitating–that here and there the intensity of the cloud shield exceeded the threshold. This interpretation is consistent with the patch of very weak radar echo encountered by the aircraft at 0950–0956 GMT.

Thus, the airborne cloud sightings, ODWs and radar observations, and the shipborne surface and upper-air observations are generally consistent with the CST-derived locations of the areas of convective and stratiform precipitation associated with cluster B. These verifications lend confidence to the derivation of total convective and stratiform rain areas and amounts from the application of the CST to the entire cluster, as discussed in the next subsection.

*c. Convective and stratiform rain areas and amounts for the entire cluster determined by the modified CST*

The areal coverage of convective, stratiform and total precipitation, and total precipitation derived from the CST applied to the complete cluster are shown in Fig. 20a. The peaks and rapid dissipation of the stratiform and total precipitation in the complete analysis lagged the convective precipitation peak and dissipation by about three hours. According to the complete CST results, the convective precipitation area grew gradually to its maximum extent of $16\times10^3$ km$^2$ at 0233 GMT on the 10th, gradually decreased for several hours, then decreased more rapidly. The stratiform precipitation area reached its maximum extent, of $68\times10^3$ km$^2$ three hours later at 0533 GMT, stayed fairly constant for several hours, then rapidly decreased. The total precipitation area, which was dominated by the stratiform area, attained its peak value of $85\times10^3$ km$^2$ at 0533 GMT in the complete analysis.

Also shown in Fig. 20a, for comparison, is the CST-derived total precipitation region from the partial analysis (from Fig. 13a). The precipitation area for the partial analysis reached its peak of $27\times10^3$ km$^2$ at 2333 GMT on the 9th, six hours earlier than the peak in the results for the complete analysis. According to the results for the complete analysis, the area of rainfall (mainly stratiform) was actually still growing at that time. The partial analysis shows a decrease in total precipitation area after 2333 GMT because the cluster moved out of the radar analysis domain. In addition, because of the inclusion of the section of the cluster (discussed in Sec. 5a) to the northeast of the Bintulu radar, the areas for the complete analysis are larger than for the partial analysis even at the beginning of the analysis time.

Percentage contributions of the areas covered by convective and stratiform rainfall to the total rainfall area are shown in Fig. 20b for both the partial and complete analyses. For the complete analysis, the contributions from the convective and stratiform components begin close to 50 % (as in the partial analysis results). The stratiform contribution grows to ~95 % by 0833 GMT on 10 December, and finally fluctuates around 90 % at the end of the life cycle. The cluster's precipitation structure during its final stage might be expected to approach 100 % stratiform. However, the CST, by construction, is unable to detect a precipitation region as 100 % stratiform, since the algorithm is "anchored" to the convective cores. Moreover, the use of the discrimination line

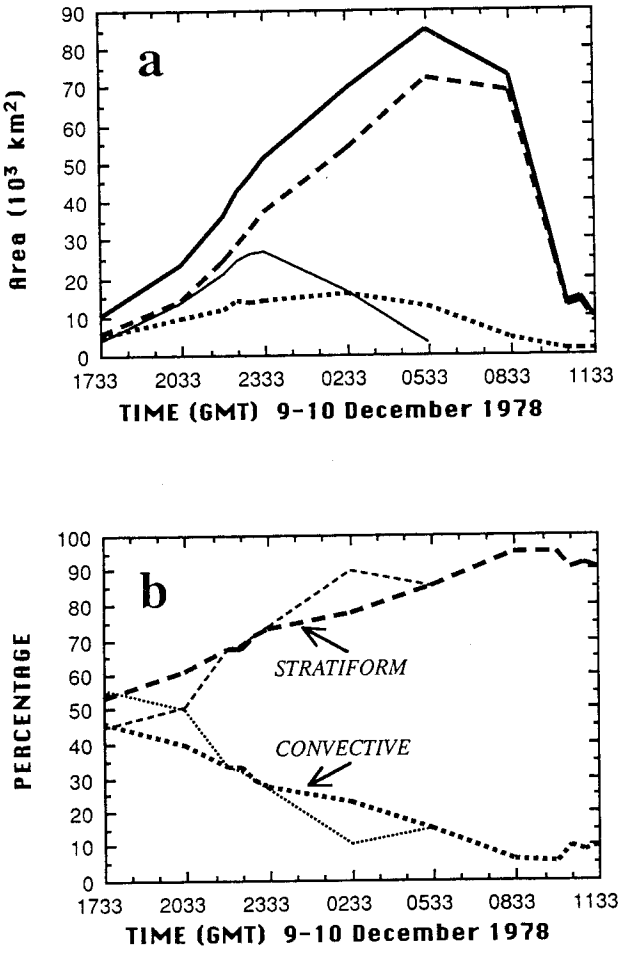


Fig. 20. (a) Convective (heavy short-dash line), stratiform (heavy long-dash line), and total (sum of convective and stratiform: heavy solid line) precipitation areas as determined by application of modified CST to complete satellite history of cluster B. The solid thin line is the total areal coverage of precipitation for the CST application over a portion of cluster B (from Fig. 13a). (b) Percent contributions to total rainfall area by the convective (short-dash lines) and stratiform (long-dash lines) precipitation regions for the CST-derived values from the complete (darker lines) and partial (lighter lines) cluster B applications.

[Eq. (3)] notwithstanding, some roughness in a decaying cirrus shield can be selected inaccurately as convective cores. However, in the case of cluster B, the CST was able to attribute almost all of the rain area to stratiform during the cluster's final stage, and these problems thus appear to be minor.

Despite large differences between the sizes of the domains covered by the complete and partial analyses and between the sizes of the total precipitation areas shown in Fig. 20a, the percentage contributions for the two components, as shown in Fig. 20b, are close. The mean difference and mean absolute difference between the results for the percentage contribution from the stratiform component for the two analyses are only about one-half and four percent, respectively, with the largest difference of 13 % occurring at 0233 GMT. This implies that the characteristics of the cluster observed in the partial analysis were fairly uniform throughout the entire cluster.

Figure 21a shows the total area-integrated rain rates for the complete CST application. As in Fig. 20a, the total results from the partial analysis are also shown (from Fig. 14a). The evolution of the convective- and stratiform-component amounts are shown in Fig. 21b. Also shown are error bars for the stratiform precipitation curve. As explained in Sec. 3f, calculations were made assuming stratiform rain rates of 1, 2, and 3 kg m$^{-2}$ h$^{-1}$. The primary results (long-dash curve in Fig. 21b) are for $\overline{R_s}$=2 kg m$^{-2}$ h$^{-1}$. The lower and upper ends of the error bars indicate how this curve would appear for 1 and 3 kg m$^{-2}$ h$^{-1}$, respectively. As in Sec. 3f, we suggest that the true stratiform rain curve probably is given best by the 2 kg m$^{-2}$ h$^{-1}$ assumption during the early through mature phases of its lifetime, but drops down toward the 1 kg m$^{-2}$ h$^{-1}$ limit during the later stages of the cluster's lifetime. Thus, the stratiform rates given by the long-dashed curve during the later stages of the cluster's lifetime (after 0400–0500 GMT) are probably overestimated somewhat.[6]

The timing of the increases, peaks, and rapid decreases shown in Figs. 21a and b generally follow the results for areal coverage shown in Fig. 20a. The main difference is that the convective component of the area-integrated rain rates is almost constant from 2233 GMT on the 9th through 0233 GMT on the 10th (the time of the peak area-integrated rain-rate value). This result arises because the peak in the average convective rain rate occurred as early as 2033 GMT (see Table 1). Therefore, the growth in areal extent of the CST-determined convective rainfall was balanced, from 2233 GMT until 0233 GMT, by the decrease in average convective rain rate (inversely related to the average cloud-top temperature associated with the convective cores; see Fig. 12). The peak convective amount at 0233 GMT was $8\times10^{10}$ kg h$^{-1}$. The peaks in the stratiform and total amounts, 14 and $20\times10^{10}$ kg h$^{-1}$, respectively, both occurred three hours later at 0533 GMT.

Percentage contributions to the total area-

[6]It is also possible that the higher values of stratiform threshold temperature in the late stages of the cluster (Fig. 16), which were not calibrated by the limited area comparison (Fig. 14), could have led to an overestimate of stratiform rain area in these later stages. However, there is no apparent physical reason why this should be so.

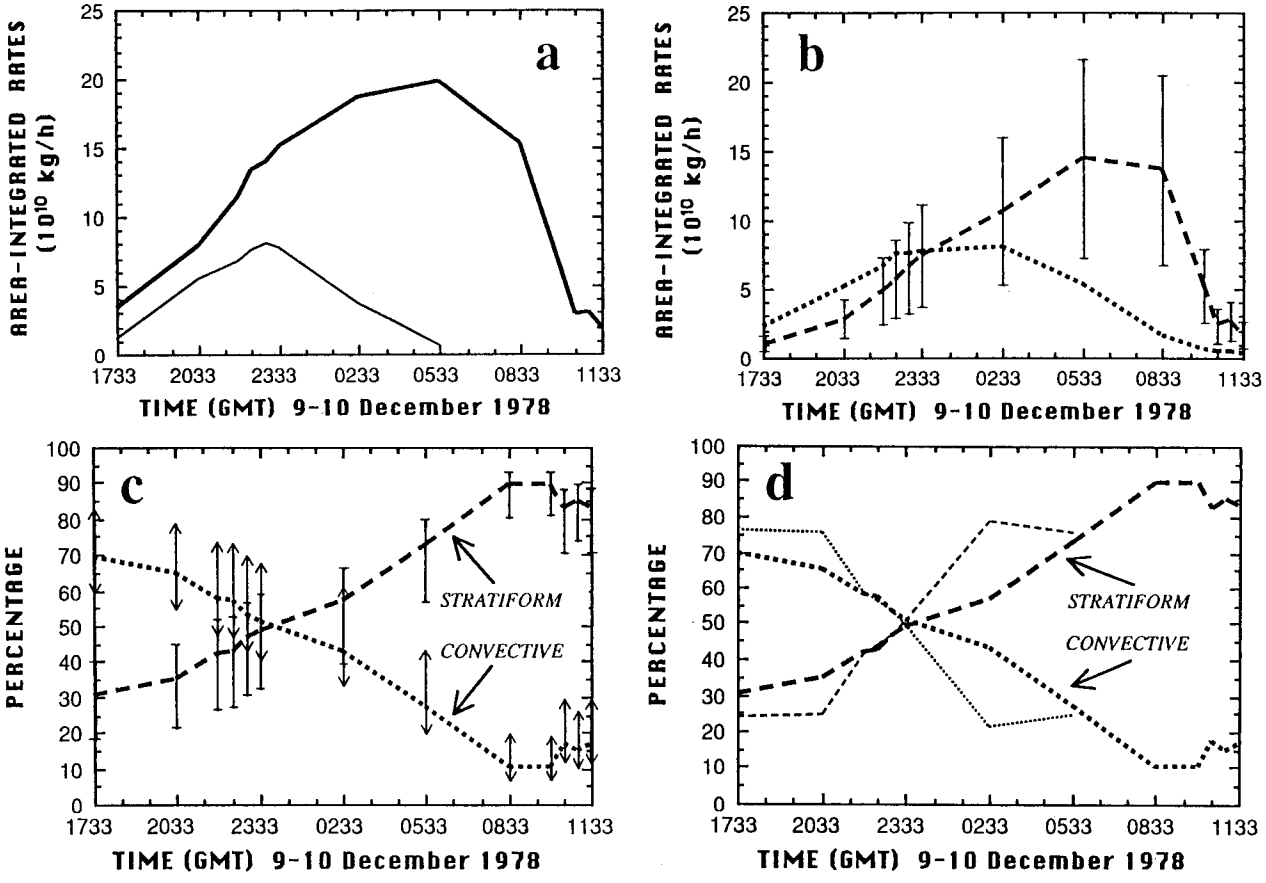


Fig. 21. (a) Total (sum of convective and stratiform) area-integrated rain rates as determined by application of modified CST to the complete satellite history of cluster B (thick solid line) and for CST application over a portion of cluster B (from Fig. 14a: thin solid line). (b) Convective (heavy short-dash line) and stratiform (heavy long-dash line) area-integrated rain rates for CST application to complete satellite history of cluster B. Lower-and upper-error bars show area-integrated rates for CST-determined stratiform component with stratiform rate set equal to 1 and 3 kg $m^{-2}$ $h^{-1}$, respectively. (c) Convective (short-dash line) and stratiform (long-dash line) percent contributions to total area-integrated rain rates. Error bars indicate percent contributions for convective and stratiform area-integrated rates when the stratiform rate is set to 1 and 3 kg $m^{-2}$ $h^{-1}$. Error-bar limits for the convective and stratiform components are given by arrowheads and horizontal lines, respectively. (d) Percent contributions to total area-integrated rain rates by the convective (short-dash lines) and stratiform (long-dash lines) precipitation regions for the CST-derived values from the complete (darker lines) and partial (lighter lines) cluster B applications.

integrated rain amounts from the convective and stratiform components of the cluster, for both the partial and complete analyses are shown in Figs. 21c and d. The stratiform rate for the curves is assumed to be 2 kg $m^{-2}$ $h^{-1}$, as in Fig. 21b. Error bars again indicate variation as $\overline{R_s}$ is varied from 1 to 3 kg $m^{-2}$ $h^{-1}$. At 1733 GMT, according to the complete analysis results, the stratiform rainfall (for $\overline{R_s}$=2 kg $m^{-2}$ $h^{-1}$) accounts for only 30 % of the precipitation for the cluster. Six hours later, at 2333 GMT, the convective and stratiform components were contributing roughly equal amounts to the overall instantaneous rainfall amount. The stratiform fractional amount continued to increase until nine hours later, when, at 0833 GMT on the 10th, it accounted for ~90 % of the total. During the time interval covered by the partial analysis, the percentage values are in fairly close agreement. Figure 21d compares the results for the partial (Sec. 4) and complete cluster B analyses. The mean difference and mean absolute difference between the stratiform results are only about one and six percent, respectively, with the greatest absolute difference of 22 % occurring at 0233 GMT.

Figures 22a and b and Fig. 23a compare the CST-determined cluster B precipitation areas with the areal extent of the cirrus shield (as defined by the 245°K threshold in the IR brightness temperature field) associated with the cluster. Figure 22a compares the cirrus shield area with the total areal of

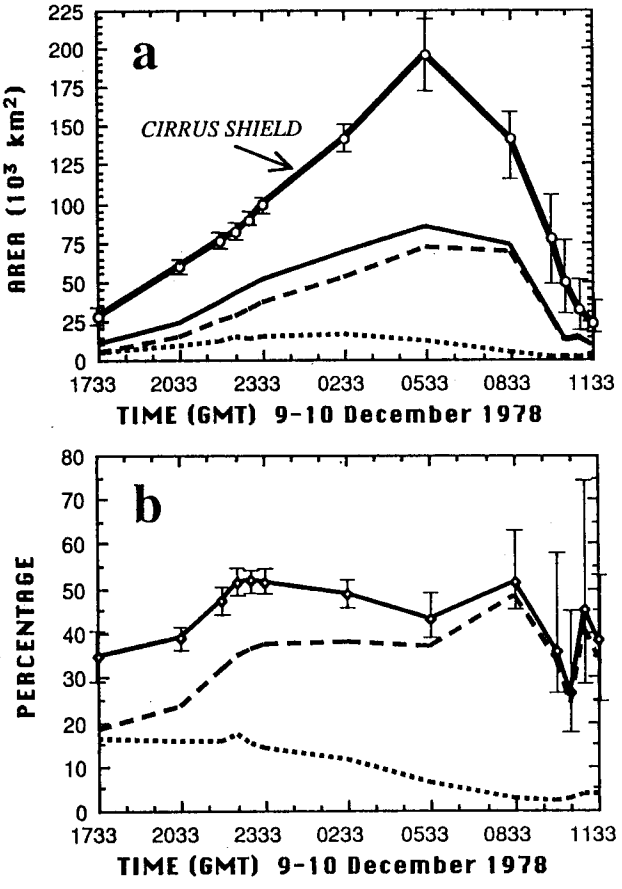


Fig. 22. (a) Areal extents of cirrus shield (defined by 245°K threshold temperature on IR satellite imagery: heaviest solid line), and CST-determined convective (short-dash line), stratiform (long-dash line) and total (sum of convective and stratiform: solid line) precipitation for complete history of cluster B. The tops and bottoms of the error bars correspond to the size of the cirrus shield area using cloud-top threshold temperatures of 250°K and 240°K, respectively. (b) Percent of cirrus shield area covered by convective (short-dash line), stratiform (long-dash line) and total (solid line) precipitation regions. Error bars on the total precipitation percentage curve correspond to error bars for the cirrus shield area shown in (a).

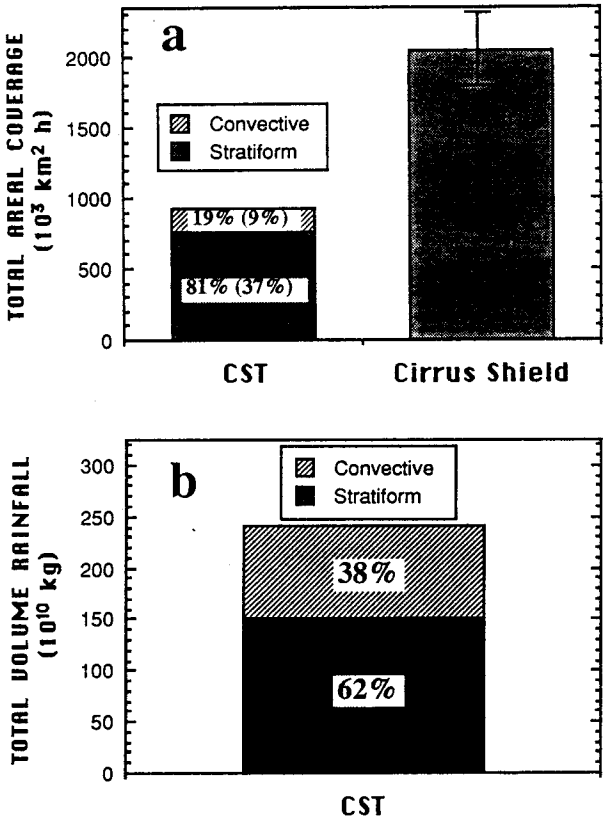


Fig. 23. Stacked column graphs for time-integrated CST-derived (a) areal coverage (from Fig. 20a) and (b) area-integrated rain rates (from Fig. 21b). Time integrations (described in the text) are for the 24 h period 1533 GMT through 1533 GMT, 9–10 December. Convective and stratiform contributions to time-integrated amounts are represented by hatched and by dark-shaded regions, respectively. Percentage contributions of the two components to the total areal coverage (a) and the total volume rainfall (b) are also included. In addition, (a) shows the time-integrated areal coverage of the cirrus cloud shield (245°K threshold). The upper and lower limits on the error bar on the total cirrus shield coverage correspond to the total coverages obtained using thresholds of 250°K and 240°K, respectively. Percentages in parentheses in (a) are the contributions of the precipitation components to the time-integrated areal coverage of the cirrus shield.

precipitation, and with the areal extent of the convective and stratiform components. Error bars are included on the curve for the cirrus shield area due to the uncertainty in accurately determining the appropriate cloud-top threshold temperature. The tops and bottoms of the error bars correspond to the size of the cirrus shield area using cloud-top threshold temperatures of 250°K and 240°K, respectively. The cirrus reached its maximum coverage of $196\times10^3$ km$^2$ at 0533 GMT, the same time as the maximum areal extent of the stratiform and total precipitation, and after a few hours diminished rapidly as the cluster dissipated.

The percentage of the cloud shield occupied by precipitation is shown in Fig. 22b. The error bars in

Fig. 22b correspond to the percentages computed, using the error bar limits from Fig. 22a. The total rainfall area filled 35–52 % of the cloud shield area with the exception of 1033 GMT on the 10th, when the coverage was only 27 %. The convective precipitation occupied a maximum of about 14–17 % of the cloud area during the first six hours of the cluster's life cycle observed by satellite. This was eventually reduced to only about 2–4 % of the cloud area. The stratiform component initially filled only 18 % of the cloud area, but eventually filled ~50 % of the cloud area at 0833 GMT before decreasing.

It is evident from Figs. 22a and b that, with the exception of 1733 GMT, the results are not extremely sensitive to the choice of cloud-top threshold temperature until 0533 GMT. At the earlier times, the cloud shield edges tended to be sharper, with strong temperature gradients. Therefore, a relatively wide band of threshold temperatures produces similar results for area. However, as the cluster begins to dissipate, the edges are less well-defined and selection of an appropriate threshold temperature becomes more difficult. Before 0533 GMT, the error bars in Fig. 22b, for the variation of percentage of cirrus shield occupied by precipitation between threshold temperatures of 240°K and 250°K, are only 5–6 % (except for 11 % at 1733 GMT). At 0833 GMT, the uncertainty is 17 %. The error bars on the percentages are especially large at later times (*e.g.*, 46 % at 1103 GMT); however, the absolute areas at those times were much smaller. It could be argued that a higher threshold temperature (*i.e.*, 250°K) would be more appropriate during the cluster's dissipation period.

Figure 23 shows the time-integrated totals for the complete analysis over the entire life cycle of cluster B, the 24 h period from 1533 GMT through 1533 GMT on 9–10 December. An additional satellite image time, 1533 GMT on 9 December, has been added for the period before the beginning of the analysis just described (1733 GMT to 1133 GMT on 9–10 December) and an additional time, 1533 GMT on 10 December, after the above analysis time period, for the sake of the time integration. All values are assumed zero at those temporal boundary times. Values between these temporal boundaries and the first and last data times were determined by linear interpolation.

Figure 23a shows the time-integrated areal coverages for the cirrus cloud shield and CST-determined convective and stratiform precipitation. The time-integrated amount of the total precipitation area for cluster B is $930\times10^3$ km$^2$ h. The contributions of the convective and stratiform components are 19 % and 81 %, respectively. The inclusion of the time period after 0333 GMT in the complete analysis results, when the cluster was mainly stratiform, is responsible for the differences in the percentages between the partial and complete analysis results. The total cirrus shield coverage was $\sim2000\times10^3$ km$^2$ h using the 245°K cloud-top threshold temperature. The upper and lower error bars give the coverages using the 250°K and 240°K thresholds, respectively. In the case of the time-integrated values, the upper and lower bounds differ by only about 12 % from the value obtained using the 245°K threshold. Over the lifetime of the cluster, the total CST-determined precipitation area accounted for 46 % of the total areal coverage of the cirrus shield, of which the convective and stratiform precipitation areas accounted for 9 % and 37 %, respectively.

Figure 23b gives the total volume rainfall for cluster B. The total rainfall amount of $241\times10^{10}$ kg is partitioned into 38 % convective and 62 % stratiform rainfall. These percentages differ substantially from the 54 % convective and 46 % stratiform given earlier in this study for the partial analysis results (see Fig. 15b). As stated earlier, the larger stratiform percentage for the complete analysis results was a result of the inclusion of the latter, mainly stratiform portion of the cluster's history. Stratiform percentages given by other studies of tropical cloud clusters have ranged from 30–50 % (Houze, 1977; Cheng and Houze, 1979; Gamache and Houze, 1983; Houze and Rappaport, 1984; Leary, 1984; Wei and Houze, 1987; Chong and Hauser, 1989). The value of 62 % obtained in this study is probably a few percent too high because we assumed the 2 kg m$^{-2}$ h$^{-1}$ stratiform rain rate through the latter part of the cluster's lifetime. However, even if a correction were made by lowering the assigned value of $\overline{R_s}$ during the late stages, a value of well over 50 % would still be obtained. In addition, even if the CST-derived estimates for the areal coverage of the stratiform precipitation were overestimated for the latter stage, the effect on the total percentage contribution of stratiform precipitation would be minimal since the vast majority of the precipitation fell prior to 0533 GMT. Thus, it appears that this particular cloud cluster had a larger and/or stronger stratiform precipitation area than the other clusters reported in the literature. It has long been a subjective impression of scientists involved in WMONEX that the diurnally triggered cloud clusters off the coast of Borneo, of which cluster B was a particularly strong example, indeed had especially large and intense stratiform rain areas.

## 6. Conclusions

By applying the Convective-Stratiform Technique (CST) of Adler and Negri (1988, referred to here as AN) to a limited region of the 9–10 December 1978 Winter Monsoon Cluster B, it was possible to determine several modifications to the CST required to obtain consistency with the convective and stratiform areas determined from WMONEX radar data

by Churchill and Houze (1984a, referred to here as CH). Two particularly important changes were found to be necessary.

The first change concerns the "discrimination line," which determines whether a local minimum of satellite-observed IR temperature is identified as a convective cell. The colder the cloud top at the minimum point, the less the cell top must differ in temperature from the surroundings. In the original CST of AN, the required difference decreased linearly as the background temperature decreased. Because of the colder cloud-top temperatures in the WMONEX region, it was necessary to employ an exponential decrease, which differs little from that of AN for warmer backgrounds, but requires a much larger difference than that required in AN between cell-top temperature and the temperature of the surrounding cloud shield as the cell-top temperature decreases.

The second significant change from the version of the CST used by AN was in the assignment of a threshold temperature to define the edge of the stratiform precipitation area. For this threshold, AN used an average of the modal temperatures of the cloud-top regions surrounding the convective cellular regions. We found it necessary to add 7°K to the threshold temperature to improve agreement with the stratiform precipitation region identified in the radar analysis of CH. This empirical correction was needed because of the difference in the procedures used by AN and CH to determine the extent of the stratiform rain from radar data. AN used a higher reflectivity threshold than did CH; hence, a lower temperature threshold was required to identify the location of the rain area in the satellite data in their case.

Several other refinements were made to the technique of AN, as described in Sec. 3. However, these refinements did not substantially change the technique. To reproduce well the results of the radar analysis of CH, the basic CST is found with the two major adjustments noted above, and applied to the region of reliable quantitative radar data. The rain rates in both the convective and stratiform regions identified by the CST also agree remarkably well with the rain rates found by Leary (1984) in GATE cloud clusters.

The successful application of the adjusted CST over the limited time and space domain of the radar analysis of CH lent confidence to the application of the technique to the entire cluster over its full lifetime. Moreover, the locations of the convective and stratiform precipitation areas identified in this full analysis of the cluster were consistent with ship-based WMONEX surface and upper-air observations and WMONEX aircraft observations. The precipitation history calculated for the cluster and shown in Fig. 21b is qualitatively similar to that determined by radar for other tropical cloud clusters, *i.e.*, dominantly convective during the first few hours, reaching a peak of convective rainfall a little before the midpoint of its lifetime, and becoming dominantly stratiform while the convective component slowly decreased throughout the latter half of its lifetime. The only somewhat surprising behavior of the rain estimated in this analysis was that the stratiform amount became so large during the later stages of the cluster. The total, time and areally integrated rain was 62 % stratiform, which is higher than the 30–50 % reported in other studies. As discussed in Sec. 5c and evident from the error bars in Fig. 21b, the stratiform amount could have been somewhat overestimated during this period. However, the total in any case would appear to have been 50 % or more, indicating that this cluster was particularly effective in producing stratiform precipitation.

The successful adaption of the Adler-Negri CST to a WMONEX cloud cluster provides encouragement for future, more extensive applications of this method to equatorial cloud clusters. Satellite climatologies of cloud clusters, such as Williams and Houze (1987), can be extended to include estimates of the sizes and intensities of their internal convective and stratiform areas. The mesoscale structures of the precipitation in cloud systems can possibly be studied over broad areas of the tropics, where radar data are typically not available. The capability to infer convective and stratiform internal structure of cloud clusters from IR data will also be a valuable complement to future spaceborne precipitation radars.

## Acknowledgements

The authors thank R. Adler and A. Negri for many helpful discussions and for assistance with implementing the CST; M. Biggerstaff for an especially valuable review of the manuscript; R. Valdez and T. Rottman for compositional assistance; Grace Gudmundson for editing the manuscript; L. Callahan for technical assistance; Kay Dewar for graphics; B. Auvine of the University of Wisconsin for advice on the use of the GMS-1 data; and S. Burgsthaler and the staff of the University of Washington Microcomputer Lab for their help. This research was supported by the National Aeronautics and Space Administration under Grant NAG5-784504.

## Appendix

### *A. Revised slope parameter*

Adler and Negri (1988) specified the slope parameter, $S$, as

$$S = \frac{1}{6}(T_{i-2,j} + T_{i-1,j} + T_{i+1,j} + T_{i+2,j} + T_{i,j-1} + T_{i,j+1}) - T_{i,j}, \quad \text{(A1)}$$

where $T_{i,j}$ refers to the $T_{min}$ for which $S$ is being calculated, and the $i$ and $j$ indices refer to the east-west and north-south directions, respectively. This specification for $S$ must be modified for use with the GMS-1 satellite data because the values for $S$ as defined in (A1) are dependent on the data resolution. It is therefore necessary to account for differences between the resolutions of the GOES data (from the AN Florida study) and GMS-1 data (from the cluster B study).

To modify $S$ for the GMS-1 resolution, let $S$, as described in (A1), be seen as a measure of the "slope" (in units of °K km$^{-1}$) between $T_{min}$ and the mean of the six surrounding pixels (two each to the east and west, and one each to the north and south), multiplied by the average distance to the six pixels. Thus, (A1) can also be expressed as

$$S = \bar{\Delta}\left[\frac{\bar{T} - T_{i,j}}{\bar{\Delta}}\right], \tag{A2}$$

where

$$\begin{aligned}\bar{T} &\equiv \frac{1}{6}\left(T_{i-2,j} + T_{i-1,j} + T_{i+1,j}\right.\\ &+ \left. T_{i+2,j} + T_{i,j-1} + T_{i,j+1}\right),\end{aligned}$$

$$\begin{aligned}\bar{\Delta} &\equiv \frac{1}{6}\left[2\left(\Delta_{EW}\right) + 2\left(2\Delta_{EW}\right) + 2\left(\Delta_{NS}\right)\right]\\ &= \frac{1}{3}\left(3\Delta_{EW} + \Delta_{NS}\right).\end{aligned}$$

$\Delta_{EW}$ and $\Delta_{NS}$ are the east-west and north-south resolutions respectively, from AN, and $\bar{\Delta}$ is defined as the average distance to the six surrounding pixels. The bracketed quantity in (A2) is expressed in units of slope. Any slope calculated for the GMS-1 data would have to be multiplied by the factor outside the brackets, $\bar{\Delta}$ to be equivalent to the AN slope parameter. Letting primed variables refer to the GMS-1 data, the GMS-1 slope parameter, $S'$, can be expressed as

$$S' = \bar{\Delta}\left[\frac{\overline{T'} - T'_{i,j}}{\overline{\Delta'}}\right], \tag{A3}$$

where

$$\overline{\Delta'} \equiv \frac{1}{3}\left(3\Delta'_{EW} + \Delta'_{NS}\right).$$

One additional modification to $S'$ was made for this study. Note that in (A1) and (A3), more weight is given to the east-west differences. In addition, some information is lost by averaging the surrounding points before calculating the slopes. These two minor problems can be resolved through averaging the six different estimates for the slope, giving the same weight to the average of the four east-west estimates to the average of the two north-south estimates. This would provide a more isotropic measurement of the strength of the relative minima. For the GMS-1 data, the average of the four east-west estimates of the slope is given by

$$\begin{aligned}\overline{\text{Slope}_{EW}} = \frac{1}{4}\left[\frac{\left(T'_{i-2,j} - T'_{i,j}\right) + \left(T'_{i+2,j} - T'_{i,j}\right)}{2\Delta'_{EW}}\right.\\ \left. + \frac{\left(T'_{i-1,j} - T'_{i,j}\right) + \left(T'_{i+1,j} - T'_{i,j}\right)}{\Delta'_{EW}}\right],\end{aligned} \tag{A4}$$

and the average of the two north-south estimates is given by

$$\overline{\text{Slope}_{NS}} = \frac{1}{2}\left[\frac{\left(T'_{i,j-1} - T'_{i,j}\right) + \left(T'_{i,j+1} - T'_{i,j}\right)}{\Delta'_{NS}}\right]. \tag{A5}$$

The revised slope parameter for the GMS-1 data is then derived by replacing the bracketed quantity in (A3) by the average of (A4) and (A5) and can be expressed as

$$\begin{aligned}S' = \bar{\Delta}\left[\frac{T'_{i-2,j} + T'_{i+2,j} + 2\left(T'_{i-1,j} + T'_{i+1,j}\right) - 6T'_{i,j}}{16\Delta'_{EW}}\right.\\ \left. + \frac{T'_{i,j-1} + T'_{i,j+1} - 2T'_{i,j}}{4\Delta'_{NS}}\right].\end{aligned} \tag{A6}$$

### *B. Revised $T_{min}$ adjustment*

The adjustment applied in AN to a cloud-top temperature relative minimum, $T_{min}$, associated with a convective core, is given by

$$T_{min} - T_c(^\circ K) = \left\{\begin{array}{l} 0.283T_{min} - 56.6, \\ \quad T_{min} > 200\,K \\ 0, \\ \quad T_{min} \leq 200\,K \end{array}\right\}, \tag{B1}$$

where $T_c$ is the corrected minimum temperature. This nominal correction to $T_{min}$, which is applied to account for some of the smoothing that affects satellite-derived cloud-top temperature values due to limited spatial resolution, was deemed necessary by AN to adjust for differences between cloud-top minimum temperature values derived from results with the Adler and Mack (1984) one-dimensional cloud model, which has a horizontal grid resolution of 1 km$^2$, and cloud-top temperatures from the GOES data, which has a resolution of ~25 km$^2$. The empirical linear adjustment given in (B1) to the satellite-observed minimum temperature was obtained from a comparison of GOES and TIROS-N

AVHRR (Advanced Very High Resolution Radiometer) IR data (Negri, 1982).

For this study, the linear adjustment to $T_{min}$ is reduced by a factor of 2.5, which is the approximate ratio of the GOES to GMS-1 pixel areas. As in AN, there is no adjustment for $T_{min}$>200°K. For $T_{min}$>200°K, the new adjustment is derived by dividing the right-hand side of (B1) by the factor 2.5. The revised adjustment used for this study can then be given by

$$T_{min} - T'_c(^\circ K) = \left\{ \begin{array}{ll} 0.113T_{min} - 22.6, & \\ \quad T_{min} > 200\,K & \\ 0, & \\ \quad T_{min} \leq 200\,K & \end{array} \right\}, \quad \text{(B2)}$$

where $T'_c$c is the cloud-top temperature corrected for the difference between the GMS-1 and one-dimensional cloud model resolutions.

## References


Adler, R.F. and A.J. Negri, 1988: A satellite infrared technique to estimate tropical convective and stratiform rainfall. *J. Appl. Meteor.*, **27**, 30–51.

Adler, R.F., and R.A. Mack, 1984: Thunderstorm cloud height-rainfall rate relations for use with satellite rainfall estimation techniques. *J. Clim. Appl. Meteor.*, **23**, 280–296.

Adler, R.F., M.J. Markus and D.D. Fenn, 1985: Detection of severe mid-west thunderstorms using geosynchronous satellite data. *Mon. Wea. Rev.*, **113**, 769–781.

Cheng, C.-P. and R.A. Houze, Jr., 1979: The distribution of convective and mesoscale precipitation in GATE radar echo patterns. *Mon. Wea. Rev.*, **107**, 1370–1381.

Chong, M. and D. Hauser, 1989: A tropical squall line observed during the COPT 81 experiment in west Africa. Part II: Water budget. *Mon. Wea. Rev.*, (in press).

Churchill, D.D. and R.A. Houze, Jr., 1984a: Development and structure of winter monsoon cloud clusters on 10 December 1978. *J. Atmos. Sci.*, **41**, 933–960.

Churchill, D.D. and R.A. Houze, Jr., 1984b: Mesoscale updraft magnitude and cloud-ice content deduced from the ice budget of a tropical cloud cluster. *J. Atmos. Sci.*, **41**, 1717–1725.

Gamache, J.F. and R.A. Houze, Jr., 1982: Mesoscale air motions associated with a tropical squall line. *Mon. Wea. Rev.*, **110**, 118–135.

Gamache, J.F. and R.A. Houze, Jr., 1983: Water budget of a mesoscale convective system in the tropics. *J. Atmos. Sci.*, **40**, 1835–1850.

Gamache, J.F. and R.A. Houze, Jr., 1985: Further analysis of the composite wind and thermodynamic structure of the 12 September GATE squall line. *Mon. Wea. Rev.*, **113**, 1241–1259.

Geotis, S.G. and R.A. Houze, Jr., 1985: Rain amounts near and over North Borneo during Winter MONEX. *Mon. Wea. Rev.*, **113**, 1824–1828.

Heymsfield, G.M. and R. Fulton, 1988: Comparison of high-altitude aircraft measurements with the radar structure of an Oklahoma thunderstorm: Implications for precipitation estimation from space. *Mon. Wea. Rev.*, **116**, 1157–1174.

Houze, Jr., R.A., 1977: Structure and dynamics of a tropical squall-line system. *Mon. Wea. Rev.*, **105**, 1540–1567.

Houze, Jr., R.A., 1989: Observed structure of mesoscale convective systems and implications for large-scale heating. *Quart. J. Roy. Meteor. Soc.*, **115**, 425–461.

Houze, Jr., R.A. and A.K. Betts, 1981: Convection in GATE. *Rev. Geophys. Space Phys.*, **19**, 541–576.

Houze, Jr., R.A. and P.V. Hobbs, 1982: Organization and structure of precipitating cloud systems. *Advances in Geophysics*, **41**, 3405–3411.

Houze, Jr., R.A. and E.N. Rappaport, 1984: Air motions and precipitation structure of an early summer squall line over the eastern tropical Atlantic. *J. Atmos. Sci.*, **41**, 553–574.

Houze, Jr., R.A., S.G. Geotis, F.D. Marks Jr., D.D. Churchill and P.H. Herzegh, 1981a: Comparison of airborne-and land-based radar measurements of precipitation during Winter MONEX. *J. Appl. Meteor.*, **20**, 772–783.

Houze, Jr., R.A., S.G. Geotis, F.D. Marks Jr. and A.K. West, 1981b: Winter monsoon convection in the vicinity of North Borneo. Part I: Structure and time variation of the clouds and precipitation. *Mon. Wea. Rev.*, **109**, 1595–1614.

Hudlow, M.D., V. Patterson, P. Pytlowany, F. Richards and S. Geotis, 1979: Calibration and intercomparison of the GATE C-band weather radars. NOAA Tech. Rep. EDIS 31, 98 pp. Center for Environmental Assessment Services, NOAA, Washington, DC 20235. [NTIS PB8120305].

Johnson, R.H., 1982: Vertical motion of near-equatorial winter monsoon convection. *J. Meteor. Soc. Japan*, **60**, 682–690.

Johnson, R.H. and R.A. Houze, Jr., 1987: Precipitating cloud systems of the asian monsoon. *Monsoon Meteorology*, C.-P. Chang and T.N. Krishnamurti, Eds., Oxford University Press, New York, USA, 298–353.

Johnson, R.H. and D.L. Priegnitz, 1981: Winter monsoon convection in the vicinity of north Borneo. Part II: Effects on large-scale fields. *Mon. Wea. Rev.*, **109**, 1615–1628.

Johnson, R.J. and D.C. Kriete, 1982: Thermodynamics and circulation characteristics of winter monsoon tropical mesoscale convection. *Mon. Wea. Rev.*, **110**, 1898–1911.

Johnson, R.H. and G.S. Young, 1983: Heat and moisture budgets of tropical mesoscale and clouds. *J. Atmos. Sci.*, **40**, 2138–2147.

Julian, P.R., 1982: The aircraft dropwindsonde system in the global weather experiment. *Bull. Amer. Meteor. Soc.*, **63**, 619–627.

Leary, C.A, 1984: Precipitation structure of the cloud clusters in a tropical easterly wave. *Mon. Wea. Rev.*, **112**, 313–325.

Leary, C.A. and E.N. Rappaport, 1987: The life cycle and internal structure of a mesoscale convective complex. *Mon. Wea. Rev.*, **115**, 1503–1527.

Maddox, R.A., 1980: An objective technique for separat-

ing macroscale and mesoscale features in meteorological data. *Mon. Wea. Rev.*, **108**, 1108–1121.

Martin, D.W. and A.J. Schreiner, 1981: Characteristics of west African and east Atlantic cloud clusters: A survey from GATE. *Mon. Wea. Rev.*, **109**, 1671–1688.

Martin, D.W. and M.R. Howland, 1986: Grid history: A geostationary satellite technique for estimating daily rainfall in the tropics. *J. Clim. Appl. Meteor.*, **25**, 184–195.

Negri, A.J., 1982: Cloud-top structure of tornadic storms on 10 April 1979 from rapid scan and stereo satellite observations. *Bull. Amer. Meteor. Soc.*, **63**, 1151–1159.

Simpson, J., R.F. Adler and G.R. North, 1988: A proposed tropical rainfall measuring mission (TRMM) satellite. *Bull. Amer. Meteor. Soc.*, **69**, 278–295.

Szoke, E.J., E.J. Zipser and D.P. Jorgensen, 1986: A radar study of convective cells in mesoscale systems in GATE. Part I: Vertical profile statistics and comparison with hurricanes. *J. Atmos. Sci.*, **43**, 182–197.

Szoke, E.J. and E.J. Zipser, 1986: A radar study of convective cells in mesoscale systems in GATE. Part II: Life cycles of convective cells. *J. Atmos. Sci.*, **43**, 199–218.

Warner, C., 1982: Mesoscale features and cloud organization on 10-12 December 1978 over the South China Sea. *J. Atmos. Sci.*, **39**, 1619–1641.

Wei, T. and R.A. Houze, Jr., 1987: The GATE squall line of 9–10 August 1974. *Adv. Atmos. Sci.*, **4**, 85–92.

Williams, M. and R.A. Houze, Jr., 1987: Satellite-observed characteristics of winter monsoon cloud clusters. *Mon. Wea. Rev.*, **115**, 505–519.

Zhang, D.-L. and J.M. Fritsch, 1988: Numerical sensitivity experiments of varying model physics on the structure, evolution and dynamics of two mesoscale convective systems. *J. Atmos. Sci.*, **45**, 261–293.

Zipser, E.J., 1977: Mesoscale and convective-scale downdrafts as distinct components of squall-line circulation. *Mon. Wea. Rev.*, **105**, 1568–1589.

Zipser, E.J., 1988: The evolution of mesoscale convective systems: Evidence from radar and satellite observations. *Tropical Rainfall Measurements,* J.S. Theon and N. Fugono, Eds., A. Deepak Publ., Hampton, Virginia, USA, 159–166.

# 静止衛星赤外データから決定した冬季モンスーン雲クラスターの対流性及び層状性成分

**S.B. Goldenberg, R.A. Houze Jr., and D.D. Churchill**

(Department of Atmospheric Sciences, University of Washington)

Adler と Negri(1988) によって創案された、メソスケール対流性雲システムからの対流性及び層状性降水の面積と量を赤外衛星画像から見積る技法を、冬季モンスーン実験 (WMONEX) 期間中に南シナ海上で観測された大きな雲クラスターに適用した。その際、このクラスターの限られた部分で得られた地上レーダーデータのこれまで行った解析との一致を得るために、この技法に修正を加えた。この修正は、衛星データにおいて対流性セルと認定する方法を WMONEX 領域に特徴的な極めて冷たい雲頂温度を説明するように変更したこと、層状性雨領域の境界に対する赤外温度しきい値を修正したことなどである。

このクラスター領域と存続期間の限られた部分においてレーダー解析との一致を得た後に、この衛星データ解析法をクラスター全体について全存続期間にわたって適用した。この拡張された解析により見出された対流性及び層状性雨域面積は、WMONEX 研究観測船及び航空機によるクラスターの観測と一般的に一致している。このクラスターの存続期間にわたっての衛星解析によって示された全対流性及び層状性降水の盛衰は他の赤道域雲クラスターについてこれまで行われたレーダー解析と定性的には一致するが、このクラスターはその最盛期において特に強い層状性成分を発達させているように見える。

Adler と Negri の技法の WMONEX 雲クラスターへの適用の成功は、レーダーデータを典型的には利用できない熱帯の大きな領域にわたって、雲クラスターの対流性・層状性内部構造についての衛星にもとづく気候学を発展させることを激励するものである。この技法はまた、将来の衛星搭載降水測定レーダーシステムへの有用な補足手段となるように見える。